Wall-Modeled Large-Eddy Simulations For NASA's Jet Noise Consensus Database Of Single-Flow, Round, Convergent Jets

Gerrit-Daniel Stich *, Aditya S. Ghate †, Jeffrey A. Housman ‡ and Cetin C. Kiris §
NASA Ames Research Center, M/S 258-2, Moffet Field, CA 94035

A campaign of wall-modeled large-eddy simulations (WMLES) using structured curvilinear overlapping grids has been performed with the Launch Ascent and Vehicle Aerodynamics (LAVA) computational fluid dynamics (CFD) software to predict jet noise for single-stream axisymmetric round jets. The simulations address the new Prediction Uncertainty Reduction (PUR) technical challenge within the context of NASA's Commercial Supersonic Technology (CST) project. The goal of PUR is to quantify and reduce uncertainties from scale-resolving simulations to assess noise characteristics of next generation quiet supersonic commercial jets during takeoff and landing conditions where the noise from the exhaust jet dominates. The focus of this effort is to generate a simulation database for single-stream axisymmetric round nozzles at several conditions both for static (no ambient co-flow), which is the focus of this article, and in-flight (flight stream co-flow) conditions, which are beyond the current scope. Nine different flow conditions ranging in jet exit Mach number from 0.38 to 1.0 with nozzle temperature ratios (NTR) from 0.84 to 2.7 have been conducted. Details of the structured overset grids, numerical discretization and wall-model are provided. Near-field comparisons to PIV data show great agreement for both velocity and normal stresses, however a systematic TKE overshoot at the nozzle exit is seen in the lipline shear-layer. A permeable Ffowcs Williams Hawkings (FWH) surface, enclosing the jet, is used to predict far-field noise from the simulated flow-field. Comparison of CFD predictions to microphone array measurements demonstrate excellent agreement within the resolved frequency range. A systematic under-prediction of far-aft observer angles larger than 150 degrees has been observed across all simulations. We achieved a cost reduction of an order of magnitude for these WMLES compared to an earlier study of this configuration due to algorithmic and software improvements. The accuracy of the results and short turnaround time demonstrate that WMLES within the LAVA framework is a cost-effective approach for jet noise predictions that could soon be incorporated into the design cycle of jet noise reduction technologies.

I. Introduction

NASA's Commercial Supersonic Technology (CST) project has formulated a technical challenge to design a quiet propulsion system for a low boom supersonic aircraft that meets Federal Aviation Authority's airport noise regulations with sufficient margin. In recent years, two distinct approaches are being investigated to reduce jet noise. One approach is optimizing the nozzle geometries to increase turbulent mixing [1–3]. The other approach is to take advantage of shielding from the airframe by using novel integrated propulsion concepts [4, 5]. An approach that combines both complementary ways of reducing jet noise targeting enhanced turbulent mixing through devices such as chevrons and shielding through radical installation concepts will most likely be necessary to address the significant challenges posed by airport noise regulations for commercial supersonic aircraft[6, 7]. Within this context, the development of carefully validated computational tools to evaluate proposed concepts for low noise propulsion is a key pacing item. Another key challenge is the systematic assessment of additional noise from the interaction between high-speed jet turbulence and a surface in its vicinity [8, 9]. It is now widely accepted that trailing edge noise is expected to make a sizable contribution to the overall noise signature for several modern aircraft configurations that place the engine exhaust in close proximity to the airframe [10, 11]. Several future designs integrate propulsive and aerodynamic components of the aircraft even

*Science and Technology Corporation, AIAA Member, gerrit-daniel.stich@nasa.gov
†Science and Technology Corporation, AIAA Member, aditya.s.ghate@nasa.gov
‡Computational Aerosciences Branch, AIAA Senior Member, jeffrey.a.housman@nasa.gov
§Computational Aerosciences Branch, AIAA Senior Member, cetin.c.kiris@nasa.gov

closer in search of greater aerodynamic performance. Hence the issue of additional noise sources is likely to become an even more pressing concern in the future.

Jet noise predictions utilizing computational fluid dynamics (CFD) have been reported for more than four decades [12–15] and are playing an increasing role in assessing new noise reduction technologies. A review of the methods and accuracy of the simulations prior to 2008 is described in Bodony and Lele (2008) [16]. Great advancements have been made towards predicting jet noise with CFD solvers including high-fidelity simulations at flight Reynolds numbers, including simple but important geometric features such as jet surface interaction noise [17, 18]. Nevertheless most simulations reported in the literature are still limited to simple geometries and a small number of flow conditions. Due to the need for computationally demanding scale-resolving simulations to predict accurate far-field noise, it is still computationally too demanding to investigate full air frame interaction noise using the previously mentioned methods.

A possible strategy to advance towards full-scale airframe simulations including jet-noise prediction is the use of wall-modeled large eddy simulation (WMLES). In this approach, the near wall mesh does not need to resolve the high gradients near the wall, thus reducing the computational costs drastically. In order to predict jet noise on a full-scale airplane, modeling and simulation practices and the use of WMLES must be scrutinized. It is also essential to understand the uncertainties as well as the strengths and weaknesses in using WMLES as a predictive tool.

The emphasis of this work is in generating a database for jet noise predictions using wall-modeled large eddy simulation tools (WMLES) within the Launch, Ascent, and Vehicle Aerodynamics (LAVA) framework [19]. The LAVA solver can handle complex geometries, flight Mach and Reynolds numbers, and has been used for several airframe aeroacoustic problems [20–24]. Previous simulations focusing on free-jet noise and jet surface interaction noise have been carried out with excellent agreement [17, 25, 26].

More recently, several publications utilizing WMLES for the prediction of jet noise for a variety of flow configurations have been published [13, 27–30]. Additional examples where WMLES has been applied to multiple configurations can be found in Liu *et al.* [31], where two configurations of a supersonic cold jet at under-expanded and over-expanded conditions are investigated. Chauhan *et al.* [32] have also utilized WMLES using a discontinuous Galerkin method on a two-stream supersonic nozzle configuration. However, to our best knowledge no attempt has been made so far in generating a database for the same nozzle geometry over a range of different flow conditions in order to assess the uncertainties of these scale-resolving simulation methods for jet noise predictions.

As a first step towards addressing and quantifying the uncertainties of jet noise simulations, a Technical Challenge called Prediction Uncertainty Reduction (PUR) [1] has been created within NASA's Commercial Supersonic Technology (CST) project. To achieve this technical challenge, physics-based simulations (PBS) are utilized to generate a database for both static ambient conditions with zero free-stream co-flow and in-flight conditions with a realistic free-stream Mach number. The simulation data is then validated against NASA experimental rig benchmark data for single-flow and multi-stream nozzles. This paper will only focus on the static conditions for a single-stream axisymmetric nozzle. Nine different set points (SP) where simulated and compared against NASA experimental rig data. A single mesh was utilized for all simulations in order to reduce uncertainties from mesh differences. Near-field statistics at the centerline and lipline are compared with dedicated experiments conducted at NASA Glenn Research Center. A permeable Ffowcs Williams-Hawkings (FWH) surface, enclosing the jet is used to predict far-field noise from the simulated flow-field. Comparisons are made with microphone array data between observer angles of 55 to 165 degrees in increments of 5 degrees.

II. Problem Description

The corresponding experiments were conducted at the Small Hot Jet Acoustic Rig (SHJAR), which is located in the Aeroacoustic Propulsion Laboratory (AAPL) at NASA Glenn Research Center [3, 33, 34]. Figure 1 (a) shows a perspective picture of the SHJAR including the test nozzle and microphone layout with 24 microphones on the left side of the image. Note that the nozzle axis in the downstream flow direction is marked as 180° in the experimental coordinate system. The SHJAR was commissioned in 2001 to test jet noise reduction concepts and develop advanced measurement techniques and is capable of supplying air at flow rates up to 2.7 kg/s to a single-nozzle stream. Details of the SHJAR, the measurement techniques used to acquire the near-field and far-field data, and validation of experimental results are presented in [8, 35, 36]. As propulsion noise is the primary source of sound during take-off, flight conditions between $0.5 \leq M \leq 0.9$ where considered in the experiments. The baseline single stream Small Metal Chevron (SMC) nozzle, shown in Figure 1 is used for the current study. It has been stripped of all drill holes and additional attachment hardware to simplify meshing. The SMC nozzle has an exit diameter of 2". The purpose of this ongoing work is to

generate a numerical database of scale-resolving WMLES simulations for a variety of flow conditions in order to assess uncertainties of WMLES for jet noise predictions. These include configurations for both static ($M_{ref} \approx 0$) as well as in-flight ($M_{ref} > 0$) reference conditions. No experiments with in-flight conditions using the SMC000 2 inch nozzle were performed. However it has been identified that experiments on the C4-S1-P1+ext NATAR rig (Figure 2(b)) which consists of a 4 inch nozzle result in very comparable noise predictions. As the purpose is to minimize grid effects during the database generation, we opted to use the same mesh for all simulations instead of adjusting the mesh for geometric changes. For this reason a slight modification was made to the geometry and an outer sleeve was added to the baseline SMC000 nozzle with 12 inch extension. This was achieved by extending the outer SMC geometry with a 11deg cone (Figure 2(a)) to match the outer geometry of the C4 nozzle (Figure 2(b)). Previous simulations performed by the authors [17, 25, 26] in combination with this study confirm that the geometric modifications have no significant effect on far-field noise predictions for static flow conditions. The outer geometry will be of bigger significance for in-flight conditions as a the added outer stream will result in a boundary layer several nozzle diameters thick. This will have an effect on the velocity gradient at the nozzle exit. However results obtained with in-flight conditions are not part of this publication and will be presented in the future. Table 3 list the test conditions presented in this paper. Near-field PIV data and far-field microphone data acquired in the SHJAR for the SMC as well as C4 nozzle were provided by NASA Glenn Research Center for validation [3, 33].

Table 1 Definition of test conditions. Ma - acoustic mach number, M_j - jet exit mach number at centerline, NPR - nozzle pressure ratio, NTR - nozzle temperature ratio, X_C - potential core length chosen in experiments to collapse peak centerline turbulence across all SP.

Set Point	Ma	M_j	NPR	NTR	P_t	T_t	U_{jet}	X_c/D_j	Exp. Data	
SP	[-]	[-]	[-]	[-]	[psi]	[R]	[m/s]	[-]	PIV	MIC
3	0.50	0.51	1.197	0.96	17.138	535.2	173	5.10	✓	✓
7	0.90	0.98	1.852	0.84	26.516	521.5	306	6.02	✓	✓
23	0.50	0.38	1.102	1.76	15.778	960.5	171	3.85	✓	✓
27	0.90	0.68	1.368	1.76	19.526	1029.5	313	4.32	✓	✓
29	1.33	1.00	1.898	1.76	27.090	1133.6	460	4.94	✓	✓
38	1.33	0.88	1.664	2.27	23.745	1400.7	460	-	✗	✓
46	0.90	0.56	1.219	2.70	17.453	1513.2	305	3.62	✓	✓
49	1.48	0.90	1.697	2.70	24.219	1673.4	512	4.25	✓	✓
101240	1.14	0.85	1.608	1.78	23.080	1086.1	392	-	✗	✓

III. Computational Methodology

The LAVA solver framework [19] is utilized for the computational study. LAVA offers flexible meshing options and was developed with the intent of modeling highly complex geometry and flow-fields. The framework supports Cartesian and curvilinear structured grids as well as unstructured arbitrary polyhedral meshes. For this work the compressible Navier-Stokes equations are solved using a finite-difference formulation applied to the curvilinear transformed system of equations in strong conservation law form using a 3rd order RK3-TVD time integration scheme [37]. Overset grid technology [38] is used to couple the solutions across different overlapping meshes. In this study, the structured curvilinear overlapping grid methodology is used with a WMLES approach. The curvilinear overset grids are generated utilizing the Pointwise^{TM} and Chimera Grid Tools (CGT) [39] software packages.

A. Low dissipation finite-fifference method

High-order accurate, low dissipation finite-difference schemes have been shown to be an accurate and efficient strategy for turbulence resolving simulations using LAVA [20, 23, 40, 41] . A thorough study comparing several high-order finite difference methods on Cartesian grids within the LAVA framework was reported previously [42]. Results from this study indicated that high-order Weighted Essentially Non-Oscillatory (WENO) schemes [43] performed well in both resolution (Points-Per-Wavelength PPW), shock capturing, and robustness under harsh flow conditions.

A natural extension of finite-difference WENO schemes to curvilinear grids are the high-order Weighted Compact Nonlinear Schemes (WCNS)[44–46]. The WCNS method, applied to the convective fluxes, consists of a WENO or high-order interpolation (as opposed to reconstruction) of the left and right states to the half grid points, followed by an evaluation of the numerical flux at the half points by an approximate (or exact) Riemann solver or flux vector splitting scheme, and concluding with a high-order central finite-difference operator at the grid points which depends on the numerical fluxes at the half points in either an implicit (i.e. compact) or explicit form. When applying finite-difference methods to the curvilinear equations in strong conservation law form, standard WENO finite-difference methods will not satisfy the Geometric Conservation Law (GCL) making it necessary to combine the WENO interpolation with high-order central-difference operators. It has been shown that free-stream preservation (i.e. the GCL condition) is satisfied up to machine precision provided that identical central difference operators are used for discretizing the metric terms as well as the fluxes [47]. An additional advantage of WCNS over WENO is the ability to use approximate Riemann solvers. Standard finite-difference WENO methods require the use of flux vector splitting methods for numerical flux evaluation. In this work, a modified version of the Roe numerical flux is used [48]. A consequence of using high-order central difference operators applied to numerical fluxes at the half grid points, which depend on high-order left and right state interpolations, is a much wider stencil required for the same order of accuracy compared to standard nodal finite-difference methods. To remove this pathology, high-order central difference operators using a combination of the numerical fluxes at the half grid points and the physical fluxes at the grid points have been developed [49, 50].This approach, denoted Hybrid Weighted Compact Nonlinear Scheme (HWCNS), allows for up to third/fourth-order accuracy using a five-point stencil by combining blended third- and fourth-order interpolation with a fourth-order hybrid central difference operator. The blending of an upwind biased and pure central variable reconstruction [51], has been generalized by the authors to variable interpolation. A detailed description of the implementation in LAVA is included in the appendix of Housman et al. [52].

In the current approach, the convective fluxes (and the metric-terms used within) are evaluated using mid-point central differencing operators with variable interpolation using a shock-sensor based blending between 3rd order WENO interpolation and 4th order central interpolation. Explicit RK3-TVD [37] is used for physical time-integration with a CFL restriction of 1.25. Finally, a masking of the blended interpolation (of 50% 3rd order upwind and 50% 4th order central) is performed near overset fringe points to enhance robustness and reduce numerical artifacts which may occur near overset boundaries using low dissipation schemes. This is especially crucial for acoustic predictions as spurious oscillations at an overset interface can corrupt the far-field noise signal.

B. Wall-treatment for scale resolving simulation

The work presented in this paper uses an equilibrium wall model (no separate embedded wall-parallel grid necessary) with the analytic wall-function of Musker [53] to evaluate the wall-shear stress using the velocity at the matching location. Due to the low-Mach number character of the flow (and therefore lack of significant compressibility within the boundary layer), along with adiabatic treatment of the wall, the use of an analytic wall-function offers a computationally efficient alternative to solving the wall-normal ODEs derived from the thin boundary layer equations. Bocquet et al. (2012) [54], among others (see review by Larsson *et al.* [55]) have argued that for the flow regime being considered the analytic/algebraic wall-model and the ODE-based wall model are essentially identical in terms of accuracy.

The velocity supplied into the wall-model is taken from the second off-wall point[55] and the returned wall-shear stress is used as a viscous flux boundary condition to the PDE solved at the first off-wall point after appropriate tensor rotations based on the rotation from local curvilinear coordinates to wall coordinates. The constant coefficient Vreman model[56] serves as the subgrid-scale closure and a constant value of 0.08 is used in all simulations. For further information regarding WMLES, including a discussion on the applicability of an Equilibrium WM for non-equilibrium separated flows, the reader is referred to the recent reviews by Larsson et al. (2016)[55] and Bose & Park (2018) [57].

For a more recent application of the wall-model within the LAVA solver and additional information on the numerical method, see Ghate *et.al* [24, 40, 41, 58] where the wall-model is applied to the NASA juncture flow experiment (JFM), the NASA high speed Common Research Model (HS-CRM) for transonic flows, and the NASA high-lift Common Research Model.

C. Turbulent inflow generation

The noise produced by attached boundary layers, such as the boundary layer near a nozzle exit, are highly dependent on the 3D turbulent structures near the wall. These turbulent structures also significantly influence the development

of the turbulent jet shear layers emanating from the nozzle exit which dictate the accuracy of the far-field acoustic prediction [59]. Non-zonal methods, such as DDES, are known to be less accurate for these types of flows, and only Direct Numerical Simulation (DNS) and wall-resolved LES are truly capable of modeling these turbulent structures deep in the boundary layer [60]. Since wall-resolved LES of even small portions of the nozzle interior, near the nozzle exit, are still not affordable for realistic Reynolds numbers, an alternative strategy must be leveraged. The approach we chose is to utilize WMLES [27, 59, 61] which substantially reduces the meshing requirements compared to wall-resolved LES. The equilibrium wall model described above is used in the nozzle interior upstream of the nozzle exit. Since no turbulent fluctuations are resolved in the upstream slip section from the nozzle inflow until the wall-modeled section (see Figure 3), artificial turbulent fluctuations are needed to stimulate the development of resolved turbulent structures in the boundary layer. Tripping dots are added to create these fluctuations. An example of such an array of tripping dots was shown in Stich *et al.* [26]. The tripping dots are treated with an immersed boundary penalty method which applies a source term to the momentum equations. The tripping dots' height is commensurate with that of the first point off the wall in order to have minimal effects on the mass flow rate and boundary layer thickness. A staggered tripping dot configuration is used with 144 equidistant tripping dots per row. Previous simulations have shown that this method has a smaller impact on the far-field noise spectra compared to a classical synthetic eddy method like the one described in [62, 63]. A study was previously performed [26] to assess the influence of the location of the tripping dots for SP7. The tripping dots were placed at 1.5D and 5.0D upstream of the nozzle exit. No significant effect on the far-field noise was observed. This is likely due to the final convergent part 1.0D upstream of the nozzle exit which effectively resets the boundary layer thickness. The tripping location of 2.0D upstream of the nozzle exit was chosen for the present database generation effort to minimize the extent of highly refined nozzle interior mesh, and thus minimize computational cost.

IV. Structured overset meshing approach for jet noise simulations

A structured overset curvilinear grid system was created utilizing a combination of Chimera Grid Tools [39] and Pointwise™software packages. One advantage of structured overset grids for aeroacoustic analysis of jet noise is the ability to generate highly-refined, low aspect ratio grids to capture nozzle boundary layers and shear layers. Another advantage is that is allows to locally refine the meshes in the azimuthal direction at different streamwise and radial locations along the jet axis by factors of two to reduce grid size and computational cost. Structured grid flow solvers are highly efficient, have a low memory footprint, and offer a straightforward and inexpensive extension to high-order low-dissipation finite-difference discretization. Allowing the structured grids to overlap each other not only simplifies the process of generating the grids (in comparison to purely structured multi-block abutting grids), it also allows for higher quality (less-skewed, lower aspect ratio) meshes.

The meshing strategy is divided into two parts described in the following sections. A near wall mesh and a jet wake mesh. The near-wall mesh spans the nozzle and extends up to 1.0D where the overset approach is utilized to connect it to the jet wake mesh. The different mesh regions are depicted in Figure 3. The meshing approach follows guidelines presented in Boget *et.al* [64], Bres *et.al* [12, 13] as well as previous studies on jet noise using WMLES [26] as well as hybrid RANS/LES by the authors [17, 25]. Mesh details in the nozzle interior and in the wake are reported in table 2. The goal was to create a mesh that will handle multiple different flow conditions so that a single mesh system can be used for the entire CFD database generation process. The single mesh system approach is not the most cost-effective – certain conditions could be meshed with a lower cell-count based on the relevant Reynolds numbers – but it eliminates the need for further manual mesh generation and the risk of introducing grid-related uncertainties across different conditions.

A. Wall-bounded near wall mesh region

It is common practice to design a WMLES near-wall mesh based on boundary layer (BL) thickness and a minimum number of points within the BL instead of considering spacing in viscous wall units and geometric stretching ratios. The nozzle-exit BL thickness was measured from precursor RANS simulations: $\delta_{99} \approx 0.06D$. Assuming 10-20 points within the BL thickness resulted in a wall-normal spacing of $\Delta = 0.003D$.

The near-wall mesh is split into three regions with different meshing requirements depicted in Figure 3. A nozzle lip mesh (blue), a nozzle BL mesh (green) and an in-flight outer BL mesh (purple). The nozzle lip mesh has the finest resolution in order to promote a fast transition from BL turbulence inside the nozzle to shear-layer turbulence at the nozzle exit. This mesh extends from 0.5D inside of the nozzle to 1.0D downstream of the nozzle exit. Distances between grid points in this mesh are 0.0015D, 0.003D and 0.003D-0.0015D in the azimuthal, wall-normal, and streamwise

directions respectively. The wake portion of nozzle lip mesh is created by marching the front face combined with the wall-bounded mesh up to x=1.0D, where it is connected to the main part of the jet core mesh with a 5 point overlap. The maximum grid stretching never exceeds a factor of 1.02. The nozzle BL mesh is an upstream extension of the nozzle lip mesh in order to introduce additional turbulent BL content further upstream inside of the nozzle. This is depicted in Figure 3 by the green surface. In addition, an outer BL mesh was added starting at 15.0D upstream of the nozzle exit. This is necessary for in-flight conditions where BL of up to 2.0D have been observed. Apart from the outer BL mesh, this mesh is identical with the one presented in Stich *et al.* [26].

B. Jet potential core/wake mesh

The jet core/wake mesh accounts for the largest amount of the overall grid costs and contains the turbulent structures exhausted from the jet. For this study a box mesh approach was applied, where a structured box with minimal stretching in radial and streamwise direction is utilized. This approach works by defining a lower corner coordinate value (radius and streamwise location) as well as respective mesh spacings. From the beginning of each section the mesh is then stretched with a stretching ratio of less than 2% until the maximum sectional spacing is reached and kept constant from there on. A picture describing this approach and the four different sections used can be seen in Figure 4. The exact values defined for each of the sections are also listed in Table 2. This approach is fully automated and can easily be adapted to different nozzle geometries making this a highly efficient meshing approach. This method also has an added benefit of near-isotropic aspect ratio cells while conventional curvilinear approaches utilized in previous studies have increasing azimuthal distances between points further away from the nozzle centerline if the number of points in azimuth is not changed via overset.

Finally Figure 16 shows the underlying CFD mesh resolution along the conical Ffowcs-Williams Hawkins (FWH) surface triangulation. This plot can also be used to estimate the Strouhal number limit of an acceptable resolution following the analysis of Mendez *et.al* [65] and Bres *et.al* [13]. Assuming that around 8 points per wavelength are necessary with the present numerical scheme in order to have a sufficient resolution, the maximum Strouhal number can be estimated for the designed meshes with $St_{\text{lim}} = D/(8\text{V}^{(1/3)}M_{\text{jet}}a_{\text{jet}})$, where V is the cell volume at around 2. However it has been shown in previous studies that reasonable results can be achieved with fewer points per wavelength for farfield noise [17].

Table 2 Wake mesh description at different sections. Subscript lo and hi describe the lower and higher corner dimensions of the box for each section. Where x is the streamwise direction, R is the radial extent and Δ describes the near-uniform mesh spacing in all three coordinate directions. All distances and locations are normalized with jet exit nozzle diameter D.

section	x_{lo}	r_{lo}	Δ_{lo}	x_{hi}	r_{hi}	Δ_{hi}
1	0.0	1.5	0.010	5.5	-2.50	0.015
2	5.5	2.5	0.015	10.0	-2.75	0.020
3	10.0	3.0	0.020	35.0	-6.00	0.040
4	35.0	6.0	0.080	70.0	-6.00	1.500

V. Computational results

High-fidelity time-accurate simulations were performed to assess the capability of the LAVA solver with the low dissipation finite-difference method to predict jet noise accurately. All simulations utilize the equilibrium wall-modeled LES approach described in section IV. The aim of the project is to generate a database of jet-noise simulations using WMLES in order to assess the uncertainties and shortcomings of this methodology within NASA's prediction and reduction of uncertainties (PUR) technical challenge. It is also essential to complete each simulation within a reasonable turnaround time on modern computer clusters (less than 1 day). The main focus of this study is to predict far-field noise generated by single-stream axisymmetric round jets in static conditions utilizing WMLES with the aim in establishing uncertainty bounds in the future. Simulations are presented for nine different flow configurations with jet exit mach numbers ranging from 0.38 to 1.0. The nozzle temperature ratios range from 0.87 to 2.7. Exact flow conditions for each set point can be found in Table 3. A single mesh was leveraged for all simulations in order to remove mesh uncertainties

from the database generation. Only flow conditions with co-flow mach numbers close to zero will be discussed. The high frequency noise generation mainly takes place near the nozzle exit in the shear layer whereas the low frequency part of the noise is mainly generated by the interaction of turbulent structures at the end of the jet potential core at around 6D. Significant mesh resolution is required in the near-wall region in order to adequately predict the high-frequency noise associated to the fine-scale turbulent structures in the shear layer. Previous studies have shown that this is especially important in the azimuthal direction of the near-wall region. In addition near-field statistics and flow field visualizations are compared between the nine configurations and experiments.

Explicit time integration using a third order TVD RK scheme is used with a CFL of 1.25 resulting in a time step size in non-dimensional units of $dt \cdot c_\infty/D \approx 0.0005$. Steady-state wall-modeled RANS is performed on a very coarse mesh (9M) to obtain a better initial condition. This solution is then interpolated on a intermediate mesh (100M) in order to flush out transients when switching from RANS to LES. The only purpose of the intermediate mesh is to flush out transients faster as it allows a three times larger time-step size compared to the final mesh, due to a coarser mesh resolution at the nozzle lip. The bulk of the jet wake and potential core mesh is consistent between the intermediate and fine mesh. The simulation on the intermediate mesh is typically run for around 400-600 convective flow through units ($T \cdot c_\infty/D$) to flush out all transients. This time can be significantly reduced for in-flight conditions as the turbulent slow moving structures far downstream of the jet get convected with a significantly larger ambient velocity. The intermediate simulation solution then gets interpolated to the final mesh (330M) and transients are flushed out again for around 50 convective time units. Finally statistics are taken over 2000 CTUs. During the final simulation the solution gets interpolated to multiple FWH surface triangulations (see Figure 15) at a high frequency for post-processing. In addition volume data for a subset of the mesh is also generated at every 25 time steps for future post-processing analysis that is beyond the scope of this work. All simulations were performed on the NASA Advanced Supercomputing facility at NASA Ames Research Center using Intel Skylake (Electra) or AMD Rome nodes (Aitken). Additional simulation details as well as costs can be found in Table 3.

Table 3 Simulation parameters with explicit time step size Δt, total simulation time T, volume/surface output sampling frequency Δt_s and convective time unit CTU. Timings include high frequency volume output.

case name	mesh size	$\frac{\Delta r_w}{D}$	$\frac{\Delta t \cdot c_\infty}{D}$	$\frac{\Delta t_s \cdot c_\infty}{D}$	$\frac{T \cdot c_\infty}{D}$	cost (kCPUh)	CTU
present WMLES (SP7)	330M	0.0015	0.0005	0.010	2000	400	200
Stich *et al.* [26] WMLES (SP7)	220M	0.0015	0.0005	0.017	345	84	249
Stich *et al.* [17] HRLES (SP7)	210M	<0.0001	0.0070	0.06	300	298	995

A. Instantaneous flow characteristics and qualitative description

Instantaneous snapshots of streamwise velocity normalized by the jet centerline velocity for the single-stream axisymmetric jets are shown in Figures 5-7. The first location at 0.5D illustrates the detailed turbulent structures which are well captured by the simulations. The second cut is close to the breakdown of the potential core, whereas the final cut plane at 8D shows the fully mixed turbulent jet. The turbulent kinetic energy is plotted at a slice through the centerline at y=0.0. A difference in the length of the potential core and the peak TKE location along the centerline can be observed between the different cases. The location of peak turbulence along the centerline is listed in Table 3.

A comparison of the near-wall turbulent structures inside of the nozzle starting from the tripping location at x/D=-2 to the nozzle exit is displayed in Figure 8. The surface mesh at a constant distance of 0.006D has has been unrolled and the streamwise normalized velocity U/U_{jet} is displayed. This distance corresponds to the fourth mesh point off the wall for the final nozzle lip section and the second mesh point off the wall for the upstream nozzle BL region. The fine scale structures captured by the mesh inside the nozzle turbulent BL are well captured. Note that the overset mesh boundary between the nozzle BL and nozzle lip is located at -1.0D. No significant effects from this jump in resolution can be seen in the simulation. The main purpose of this refinement is to increase the circumferential resolution before the nozzle exit were the jet shear layer forms. A refinement in this region seems to be necessary in order to allow the flow to quickly transition from BL towards shear-layer turbulence. However, as discussed in Section V.B, it might still be under-resolved in order to capture the correct shear-layer turbulence in the immediate nozzle exit region. The change in velocity that can be seen at around -0.7D is related to the change in slope of the geometry. We also demonstrated in previous studies [26] that this little step in the geometry effectively resets the BL inside of the nozzle.

B. Comparison to experimental data: near-field

Near-field turbulent statistics were computed along the jet axis centerline and lipline as well as at different cross-flow planes. Comparisons are made with PIV data from the SHJAR [3]. No PIV measurements are available for two of the investigated configurations (SP38, SP101204) and therefore are not discussed in this section. Two important figures of merit are the potential core length as well as the location and magnitude of the peak turbulent kinetic energy on the jet centerline. Hence within NASA's Revolutionary Computational Aerosciences (RCA) challenge [66], which is part of NASA's CFD vision 2030 project, an improvement in the prediction of those metrics by a factor of 40% compared to state-of-the-art RANS simulations is targeted. The length of the potential core is defined as the distance at which the centerline velocity drops to 98% of the jet exit velocity. Figures 9-10 compare the time-averaged axial velocity as well as the normal Reynolds stress ($u'u'$) normalized with the nozzle exit diameter and jet centerline velocity. Comparisons are made along the centerline at y=0D and lipline at y=0.5D. In addition lines at 0.49D and 0.51D are shown to account for measurement uncertainties in the experiment close to the nozzle exit. This small variation in measurement location of 1% around the nozzle lipline leads to a strong scatter of up to 40% in measurements up to 5.0D. This scatter significantly reduces towards the breakdown of the potential core where the the lines collapse.

Across the seven observed flow configurations ranging in jet exit Mach number from 0.38 (SP23) to 1.0 (SP29) excellent agreement with experimental PIV data is observed. Capturing the length of the potential core can be very challenging. Conventional RANS simulation – with the Spalart-Allmaras one-equation turbulence model for example – typically over-predict the length of the potential core. Conversely, many CFD solvers under-predict this quantity when using scale-resolving simulations [12, 67–69]. The under-prediction is typically due to the insufficient resolution in the jet plume and the delayed transition towards turbulent structures in the nozzle shear layer. Our WMLES predictions of the length of the potential core is within 1.0% of the measured value for all conditions shown. To put this level of accuracy in perspective, the RANS simulations conducted for SP7 lead to an over-prediction of roughly 30% in the length of the potential core. The predicted decay rate of the jet centerline velocity with WMLES is also well predicted and within experimental uncertainty bounds. This demonstrates that scale resolving simulations using wall-modeled LES can fulfill the RCA challenge and show a significant improvement in the prediction of the potential core length.

Good agreement can also be observed with centerline TKE values. Both slightly early (SP7) and delayed (SP23) rise in TKE levels can be observed depending on the case. This deviation in the rise of TKE levels can be explained by the small difference in length of the potential core. No prominent trend that would tie this to either Mach number or temperature of the configuration could be gleaned. The location of the peak turbulence kinetic energy is captured well however a consistent under-prediction of the magnitude of peak turbulent kinetic energy can be observed across all simulations. This discrepancy between simulation and experiment seems to be larger for the heated configurations with NTR 1.76 (SP23, SP27 and SP29) and NTR 2.7 (SP46, SP49) compared to the cold jets NTR 0.96 (SP3) and NTR 0.84 (SP7). This is also consistent with experimental observations where a larger scatter across different experimental campaigns was observed for hot jets.

Corresponding time-average velocity and normal Reynolds stress along the lipline are presented in Figures 9-10 (column 34) along with dashed lines extracted at locations 1% above and below the lipline. Good agreement in shape and magnitude between experiment and simulation can be seen. Reliable experimental PIV measurements are not available within $x/D < 1$ due to edge effects and lack of seeding homogeneity [33]. A larger deviation from experimental results is observed in the lipline TKE values for SP7, SP27 and SP49. The WMLES simulations tend to over-predict the turbulent kinetic energy until around 3D. The reason for this trend is still under investigation. Lipline TKE levels for SP7 were described in the experimental consensus publication [33] as very challenging to predict. Some entries of the experimental campaign were also excluded from the consensus dataset. In a previous study [26] we investigated if this over-prediction is related to a scarcity of turbulent structures inside the nozzle TBL: different mechanisms were used to force flow transition upstream of the nozzle lip, by changing the resolution and virtual origins of the TBL. Multiple different variations of the virtual origin of the TBL did not result in a significant reduction of the TKE at the nozzle exit. The benchmark data shows large uncertainty bounds in this range due to the experimental measurement technique. So it is possible that the measurements are under-predicting the "true" TKE in the shear-layer near the nozzle exit. This possibility was confirmed by the experimental team responsible for the test campaign. A similar over-prediction can also be observed in the work of Ingraham *et.al* [14] for SP7.

Figure 11- 14 show radial profiles of the axial time-averaged velocity as well as the normal Reynolds stress at four different axial locations along the jet. Overall good agreement was demonstrated for all configurations. The CFD predicted spreading ratio of the jet at 4.0D tends to be slightly larger than that measured in the experiments, remains largely within the experimental uncertainty bounds.

C. Comparison to experimental data: far-field

The choice of FWH surface topology and its distance from the jet axis can significantly influence the far-field noise predictions of a given simulation. However, there is no clear consensus in the literature on where to exactly place the permeable integration surface relative to complex geometries, flow features and noise sources. Parametric studies to assess the sensitivity of far-field noise prediction to the FWH surface topology can be found in Rahier *et.al.* [70], Uzun *et.al.* [60], Shur *et.al.* [71, 72] and Bres *et.al.* [12, 13]. Choosing an appropriate FWH surface generally depends on the mesh resolution and the numerical scheme used. A trade-off has to be made between how close to the jet the FWH surface is located in order to accurately capture the waves propagating within the CFD grid while still containing all relevant noise sources. Another limiting factor on how close the surface can be to the jet is that hydrodynamic fluctuations crossing the permeable FWH surface can result in spurious contributions to the far-field noise spectra. The spurious contribution is caused by ignoring the volume integral of the quadrupole term in the FWH formulation. This can partially be addressed by using phase-averaging over the surface, which is generally done by placing appropriately spaced end-caps in the FWH surface, along the jet axis [69].

In previous works, we carefully documented the influence of different FWH surface triangulations [17, 26] for SP7. Best practices from this study were applied and a single FWH surface triangulation is utilized for all simulations for consistency. The construction of the FWH surface is also consistent with best practices outlined in Bres *et. al.* [12] and Mendez *et. al.* [65]. The permeable FWH surface triangulation used to compute the spectra follow the external nozzle shape with a consistent offset and then radially flare out at $x/D = 0$ with $y/D = 0.8$ at a slope of 0.14. This has been chosen in order to account for the different spreading ratio of the set points.

The output of the relevant surface triangulation is performed in situ during the simulation. The same tri-linear interpolation routines used in the overset solution algorithm are utilized to generate data at the FWH surface. An extremely efficient i/o procedure implemented in LAVA designed for acoustic simulations with high frequency output is utilized to write the surface triangulation data at every few time steps. This high frequency i/o procedure is fully asynchronous and barely affects the overall turnaround time. The particular formulation of the frequency-domain permeable surface FWH equations used in LAVA is similar to that presented in Lockard [73] and used for jets by Bres *et. al.* [12, 59]. As suggested in Spalart *et al.* [74] the density perturbation term is substituted in the formulation with a scaled pressure perturbation, $\rho' := \rho_\infty + p'/c_\infty^2$. The placement of the FWH surface triangulation and the use of end-caps is depicted in Figure 15. A detailed comparison of the use of end-cap averaging between 25.0D and 30.0D to remove spurious contributions from hydrodynamic pressure fluctuations crossing the FWH surface compared to an open FWH surface where both the upstream and downstream ends are extended to cover the entire domain was conducted and is reported in [12, 17]. The studies show an impact on Power Spectral Density (PSD) values for Strouhal numbers smaller than 0.5 only.

The far-field propagation is computed from the last 2.5 million time-steps (2.5e+6 $\Delta t c_\infty/D_j \approx 2000$ convective time-units) of the simulation. This is equivalent to a frequency resolution of $\Delta f \approx 3.5$ Hz with a maximum frequency of $f_{max} \approx 350,000$ Hz. This corresponds to a Strouhal number range of $St_{min} \approx 0.0006$ to $St_{max} \approx 57$. Following the procedure outlined in Refs. [12] and [59], the total time sample is sub-divided into 15 windows (or segments) with 50 percent overlap, each window has a Strouhal resolution of $\Delta St_{window} \approx 0.005$. For each time segment, a Hanning filter is applied to the time-domain FWH integrands after the mean has been subtracted, then the Fast Fourier Transform (FFT) is applied to transform the integrands into the frequency domain. The use of Hanning filter reduces spurious noise at the low frequencies caused by spectral leakage, whereas averaging over the 15 segments results in smoother (less oscillatory) spectra. Both of these post-processing methods are important for the quieter sideline angles ($\Phi < 120^\circ$). Once the FFT is complete, the FWH surface intergrals are evaluated, in the frequency domain, for each observer location to construct the acoustic pressure p'. During the calculation of the PSD, a filter correction factor of $\sqrt{8/3}$ is applied to correct for the energy lost from the Hanning filter. The PSD is then averaged independently over 72 observers in the azimuthal direction for each of the segments, which further smoothes out the spectra and helps provide higher confidence across all resolved frequencies – observer averaging of PSD over the axisymmetric direction is akin to obtain a longer signal to process at 1 observer. Finally, the 15 segments are averaged and the resulting spectrum is compared to the experimental results.

Figure 16 shows the underlying CFD mesh resolution along the conical Ffowcs-Williams Hawkins (FWH) surface triangulation. This plot can also be used to estimate the Strouhal number limit of an acceptable resolution following the analysis of Mendez *et.al* [65] and Bres *et.al* [13]. The numerical scheme requires around 8 points per wavelength in order to sufficiently resolve acoustic waves. With this assumption the maximum resolved Strouhal number can be estimated for the designed meshes as $St_{lim} = D/(8\mathrm{V}^{(1/3)} \cdot M_{\mathrm{jet}} a_{\mathrm{jet}})$ at around 2.

Figures 17-20 show the comparison of the far-field power spectral density (PSD) 100.0D away from the nozzle exit for the observers at $\Phi = 60°, 75°, 90°, 105°, 120°, 135°, 150°,$ and $160°$. Experimental data from two different campaigns is used for comparison. The first one are results from the PIV consensus database [33] the second results were supplied by James Bridges from NASA Glenn Research Center labeled GE11rdg. These were particularly supplied for SP101240 and SP38 which are not part of the consensus database. Generally a good agreement is observed in the narrow-band spectrum for all observer angles considered in this study. The peak Strouhal number is well-captured. A stronger decay for all angles past the Strouhal cutoff frequency can be observed, this trend is more pronounced for shallow angles where the mesh resolution is coarser. The use of a more isotropic mesh in the wake of the jet has also contributed to a smaller sensitivity of the placement of the FWH surface compared to previous observations [17] using a curvilinear cylindrical mesh. However this approach has been shown to be approximately 20 percent more expensive. SP3 (M_{jet}=0.5) as well as SP23 (M_{jet}=0.38) show a stronger pileup at high frequencies than the benchmark spectra for angles up to 130 degrees. This behavior has been observed in previous simulations where a synthetic eddy method (SEM) was utilized to seed turbulence inside of the nozzle which lead to a similar high-frequency pileup for SP7 [17]. This method of introducing turbulent fluctuations was more intrusive and noisy in part because it was not guaranteed to be divergence-free. Similarly, any velocity perturbations introduced by the purposely under-resolved tripping dots that deviate from the incompressible divergence-free condition will likely generate high frequency acoustics. As the jet Mach number is lowered, the overall acoustic levels drop significantly across all frequencies, and thus these spurious acoustics generated from the tripping dots become one of the dominant sources of noise at higher frequencies. Future simulations of SP3 and SP23 will be conducted using a softer and quieter transition mechanism to avoid this issue, which will likely require higher mesh resolution inside the nozzle. SP3 also shows a 'hump' in the peak-frequency at 60 degrees. The cause of this over-prediction in this otherwise well-resolved frequency range will require further investigation.

Figures 21-22 depicts the spectral directivity of far-field noise between polar angles from 55deg <= Φ <= 165deg with $\Delta\Phi$=5deg. The Strouhal number is plotted on the x-axis with the polar angle on the y-axis and the power spectral density (PSD) on the positive z-axis. To reduce the data size and complexity, the PSD values shown are third octave band-filtered: raw PSD values are integrated over each band's extents, divided by the frequency band interval, and transformed to Decibel units. The third octave center frequencies range from 200 Hz to 16kHz. Finally the absolute value of the deviation between experiment and simulation is displayed in the third column. Values of less than 1dB are displayed in blue indicating an excellent agreement between simulation and experimental database. This is the case for the majority of the observer angles. However a systematic dip in the noise spectrum at far-aft angles Φ>150deg can be observed. The 165deg observer at 100.0D away from the jet exit is likely extremely close to the turbulent flow region of the jet given the measured jet spreading ratio. Some turbulent structures far downstream of where our FWH surface ends thus could be interacting with the microphone in the experiment, but are completely ignored in the CFD. We only have sufficient mesh refinement up to 35D so it is possible that we are missing some important turbulent structures to capture the noise levels at far-aft angles for low frequencies. As these turbulent eddies are significantly larger and move on a longer time scale it is expected that the biggest impact would occur for low frequencies. Initial simulations extending the domain size to 120D have been conducted and show promising results. However these simulations are too expensive for database generation. Not only do these simulations require additional grid points to reach 120D, they also need to run an order or magnitude longer to obtain converged statistics at up to 120D.

The band-limited overall sound pressure level (OASPL) is plotted in Figure 23, where only frequencies associated with $0.08 \leq St \leq 8.0$ are considered. Excellent agreement is achieved between 120 and 150 degrees where Mach wave radiation is the dominant noise generation mechanism. At the sideline angles between 60 and 110 degrees, where the turbulence in the jet shear layer generates most of the noise, a small deviation from experiments of around 1dB to 1.5db can be observed. This is likely linked to the over-prediction of the lipline TKE at the nozzle exit. Larger under-predictions are seen in the very far aft-angles for the same reasons discussed above. Additionally it is possible that confinement effects and overall recirculation flows at the experimental facility level play a role at these angles. Further investigation of these far-aft angles is currently underway. We also note a consistent but much smaller under-prediction trend for angles smaller than 60 degree.

VI. Conclusion

A WMLES campaign using structured curvilinear overlapping grids has been performed with the LAVA CFD software to predict jet noise for single-stream axisymmetric round jets. Nine different flow conditions ranging in jet exit Mach number from 0.38 to 1.0 have been conducted. Comparisons with experiments conducted at NASA Glenn

Research Center have been made to validate the methodology, quantify its accuracy, and identify any shortcomings. Both cold and hot jet simulations were performed ranging in temperature ratio from 0.81 to 2.7. All simulations have been performed on the same mesh in order to reduce grid resolution related uncertainties. Comparison with near-field PIV and far-field microphone experimental data demonstrate overall excellent agreement with WMLES+FWH predictions. The potential core length was predicted within 1% for all conditions considered. Centerline turbulent kinetic energy magnitude as well as location were accurately predicted for all configurations. Far-field acoustic CFD predictions of the narrow band PSD compare well to experimental data in both shape and levels. Frequencies associated with Strouhal numbers ranging 0.05 to around 7 are predicted accurately. For higher frequencies, the mesh resolution is not sufficiently fine and a dropoff in spectrum is observed. Further mesh refinement would be necessary to resolve a larger Strouhal range. An alternative approach to overcome mesh resolution requirements to predict far-field noise at higher frequencies is utilization of Gabor mode enrichment [75, 76]. In this approach, which is currently being investigated for jet noise, an underlying coarse LES simulation is enriched by using spectral proper orthogonal decomposition and Gabor modes. A faster decay for higher frequencies has also been observed for far-aft angles as well as far upstream observer angles. In addition, an over-prediction of the lip-line TKE at the nozzle exit was observed. Further investigation is needed to ascertain the cause of these discrepancies with the benchmark data.

We have successfully demonstrated that predicting jet noise with WMLES inside the LAVA framework can be performed with a short-enough turnaround time to create a database in the context of NASA's Prediction Uncertainty Reduction (PUR) technical challenge. An order of magnitude reduction in computational costs has been observed for this particular solution approach compared to an earlier study using hybrid RANS/LES (HRLES) [17]. The costs for the earlier HRLES simulation for one convective flow through amounted to around 950 CPUh. For the current WMLES simulations the costs for one convective time unit are 250 CPUh, corresponding to five fold speedup. This is despite the WMLES mesh being significantly finer than the previous HRLES mesh in order to push the upper cutoff frequency limit to larger Strouhal numbers. This speedup has been achieved with a combination of algorithmic improvements as well as computer science improvements within our refactored LAVA solver framework. For example, the WMLES method allows the use of a faster explicit time-stepping integration method compared to the implicit time integration in HRLES. Since acoustic simulations often require high temporal resolution to prevent aliasing, they are particular well suited to explicit time integration methods. Each simulation was completed in less than 24 hours on 100 AMD Rome nodes. The simulations have been run for a very long time of 2000 convective time units (CTU) in order to record longer time intervals to further converge statistics and spectra and reduce uncertainty at low frequencies. From past experience, it is only necessary to record around 200-400 CTU's to obtain adequate noise predictions. This would result in turnaround times of around 2 hours. This opens the possibility of leveraging scale-resolving LES in a design process, where a number of simulations can be completed overnight and the results can be studied the following day. The next step within the PUR technical challenge is to create error metrics for jet noise predictions. For this purpose this database for static ambient conditions will be extended to include in-flight (M_{jet}=0.3) simulations.

Acknowledgments

This work was partially funded by the Commercial Supersonic Technology (CST) project under the Advanced Air Vehicles Program (AAVP) and NASA's Transformational Tools and Technologies (TTT). We would like to thank our LAVA team members for countless fruitful discussions and all the help. Our gratitude is especially extended to Gaetan Kenway who plays a crucial role in refactoring of the curvilinear LAVA solver and wall-model development. We would also like to thank your Francois Cadieux and Mahesh Natarajan for their contributions during the review process. We would also like to thank James Bridges from NASA Glenn Research Center for his support and valuable contributions in our monthly meetings. Computer time has been provided by the NASA Advanced Supercomputing (NAS) facility at NASA Ames Research Center.

References

[1] Bridges, J., "Commercial Supersonic Technology Project-Airport Noise: Prediction Uncertainty Reduction (PUR) Tech Challenge," *NASA Acoustics Technical Working Group Meeting*, 2021.

[2] Bridges, J. E., and Wernet, M. P., "Noise of Internally Mixed Exhaust Systems With External Plug For Supersonic Transport Applications," *AIAA AVIATION 2021 FORUM*, 2021, p. 2218.

[3] Bridges, J., and Brown, C., "Parametric Testing of Chevrons on Single Flow Hot Jets," Tech. Rep. NASA/TM-2004-213107, NASA Technical Manuscript, 2004.

[4] Brown, C. A., and Podboy, G., "Jet-Surface Interaction Noise from High Aspect Ratio Nozzles: Test Summary," *23rd AIAA/CEAS Aeroacoustics Conference*, 2017, p. 3522.

[5] Sengupta, G., "Analysis of jet-airframe interaction noise," *8th Aeroacoustics Conference*, 1983, p. 783.

[6] Graham, W., Hall, C., and Morales, M. V., "The potential of future aircraft technology for noise and pollutant emissions reduction," *Transport Policy*, Vol. 34, 2014, pp. 36–51.

[7] Bridges, J. E., and Wernet, M. P., "PIV measurements of a low-noise top-mounted propulsion installation for a supersonic airliner," *AIAA Scitech 2019 Forum*, 2019, p. 0252.

[8] Brown, C., "Jet-Surface Interaction Test: Far-Field Noise Results," *Proceedings of the ASME Turbo Expo 2012, Copenhagen, Denmark*, 2012.

[9] Pidboy, G., "Jet-Surface Interaction Test: Phased Array Noise Source Localization Results," *GT2012-69801*, 2012.

[10] Welge, H., Bonet, J., Magee, T., Tompkins, D., Brit, T., Nelson, C., Miller, G., Stenson, D., Stauibach, J., and Bala, N., "N plus 3 Advanced Concept Studies for Supersonic Commerical Transport Aircraft Entering Servie," *NASA/CR-2011-217084*, 2011.

[11] Kim, H., "Distributed Propulsion Vehicles," *ICAS*, 2010.

[12] Bres, G., Nichols, J., Lele, S., and Ham, F., "Towards Best Practices for Jet Noise Predictions with Unstructured Large Eddy Simulations," *42nd AIAA Fluid Dynamics Conference, New Orleans, Louisiana*, 2012. AIAA-2012-2965.

[13] Bres, G., Jordan, P., Jaunet, V., Ke Rallic, M., Cavalieri, A., Towne, A., Lele, S., Colonius, T., and Schmidt, O., "Importance of nozzle-exit boundary-layer state in subsonic turbulent jets," *Journal of Fluid Mechanics*, Vol. 851, 2018, pp. 83–124.

[14] Ingraham, D., and Bridges, J., "Validating a Monotonically-Integrated Large Eddy Simulation Code for Subsonic Jet Acoustics," *55th AIAA Aerospace Sciences Meeting, Grapevine, Texas*, 2017. AIAA-2017-0456.

[15] Jordan, P., and Colonius, T., "Wave Packets and Turbulent Jet Noise," *Annual Review of Fluid Mechanics*, Vol. 45, 2013, pp. 173–195.

[16] Bodony, D., and Lele, S., "Current Status of Jet Noise Predictions Using Large-Eddy Simulation," *AIAA Journal*, Vol. 46, No. 2, 2008, pp. 364–380.

[17] Stich, G.-D., Housman, J. A., Kocheemoolayil, J. G., Kiris, C. C., and Bridges, J. E., "Large-Eddy Simulation of Jet Surface Interaction Noise," *25th AIAA/CEAS Aeroacoustics Conference*, 2019, p. 2475.

[18] Paliath, U., and Premasuthan, S., "Large eddy simulation for jet installation effects," *19th AIAA/CEAS Aeroacoustics Conference*, 2013, p. 2137.

[19] Kiris, C., Housman, J., Barad, M., Brehm, C., Sozer, E., and Moini-Yekta, S., "Computational Framework for Launch, Ascent, and Vehicle Aerodynamics (LAVA)," *Aerospace Science and Technology*, Vol. 55, 2016, pp. 189–219.

[20] Housman, J., Stich, G., and Kiris, C., "Predictions of Slat Noise from the 30P30N at High Angles of Attack using Zonal Hybrid RANS-LES," *AIAA/CEAS Aeroacoustics Conference*, 2019.

[21] Barad, M., Kocheemoolayil, J., and Kiris, C., "Lattice Boltzmann and Navier-Stokes Cartesian CFD Approaches for Airframe Noise Predictions," *AIAA Aviation Forum*, Vol. 23, 2017.

[22] Housman, J., and Kiris, C., "Structured Overlapping Grid Simulations of Contra-Rotating Open Rotor Noise," *54th AIAA Aerospace Sciences Meeting*, 2016. AIAA-2016-0814.

[23] Stich, G.-D., Housman, J., Kocheemoolayil, J., Barad, M., and Kiris, C., "Application of Lattice Boltzmann and Navier-Stokes Methods to NASA's Wall Mounted Hump," *AIAA Aviation Forum, Atlanta, Georgia*, 2018.

[24] Ghate, A. S., Kenway, G. K., Stich, G.-D., Browne, O. M., Housman, J. A., and Kiris, C. C., "Transonic lift and drag predictions using Wall-Modelled Large Eddy Simulations," *AIAA Scitech 2021 Forum*, 2021, p. 1439.

[25] Housman, J., Stich, G., and Kiris, C., "Jet Noise Prediction using Hybrid RANS/LES with Structured Overset Grids," *23rd AIAA/CEAS Aeroacoustic Conference, Denver, Colorado*, 2017. AIAA-2017-3213.

[26] Stich, G.-D., Housman, J. A., Ghate, A. S., and Kiris, C. C., "Jet Noise Prediction with Large-Eddy Simulation for Chevron Nozzle Flows," *AIAA Scitech 2021 Forum*, 2021, p. 1185.

[27] Aikens, K., Dhamankar, N., Martha, C., Situ, Y., Blaisdell, G., Lyrintzis, A., and Li, Z., "Equilibrium Wall Model for Large Eddy Simulations of Jets for Aeroacoustics," *52nd AIAA Aerospace Sciences Meeting, National Harbor, Maryland*, 2014. AIAA-2014-0180.

[28] Brès, G. A., Ham, F., Nichols, J. W., and Lele, S. K., "Nozzle wall modeling in unstructured large eddy simulations for hot supersonic jet predictions," *19th AIAA/CEAS Aeroacoustics Conference*, 2013, p. 2142.

[29] Le Bras, S., Deniau, H., Bogey, C., and Daviller, G., "Development of compressible large-eddy simulations combining high-order schemes and wall modeling," *AIAA Journal*, Vol. 55, No. 4, 2017, pp. 1152–1163.

[30] Liu, J., "Large-Eddy Simulations of Nozzle-Exit Conditions in Subsonic Jet Flows," Tech. rep., NAVAL RESEARCH LAB WASHINGTON DC WASHINGTON United States, 2020.

[31] Liu, J., and Corrigan, A. T., "Large-eddy simulations of supersonic jet noise generation using wall modeling," *2018 AIAA/CEAS Aeroacoustics Conference*, 2018, p. 3943.

[32] Chauhan, M., and Massa, L., "Large-Eddy Simulation of Supersonic Jet Noise with Discontinuous Galerkin Methods," *AIAA Journal*, 2021, pp. 1–20.

[33] Bridges, J., and Wernet, M., "The NASA Subsonic Jet Particle Image Velocimetry (PIV) Dataset," Technical Memorandum NASA-TM-2011-216807, National Aeronautics and Space Administration, 2011.

[34] Bridges, J., and Brown, C., "Validation of the Small Hot Jet Acoustic Rig for Jet Noise Research," Tech. Rep. AIAA 2005-2846, AIAA, 2005.

[35] Brown, C., and Wernet, M., "Jet-Surface Interaction Test: Flow Measurement Results," *20th AIAA/CEAS Aeroacoustics Conference*, 2014. AIAA 2014-3198.

[36] Brown, C., and Bridges, J., "Small Hot Jet Acoustic Rig Validation," Technical Memorandum NASA-TM-2006-214234, National Aeronautics and Space Administration, 2006.

[37] Gottlieb, S., and Shu, C.-W., "Total variation diminishing Runge-Kutta schemes," *Mathematics of computation*, Vol. 67, No. 221, 1998, pp. 73–85.

[38] Steger, J., and Benek, J., "On the Use of Composite Grid Schemes in Computational Aerodynamics," Technical Memorandum 88372, NASA, 1986.

[39] Chan, W., "Developments in Strategies and Software Tools for Overset Structured Grid Generation and Connectivity," *20th AIAA Computational Fluid Dynamics Conference, Honolulu, Hawaii*, 2011. AIAA-2011-3051.

[40] Ghate, A. S., Housman, J. A., Stich, G.-D., Kenway, G., and Kiris, C. C., "Scale Resolving Simulations of the NASA Juncture Flow Model using the LAVA Solver," *AIAA Aviation 2020 Forum*, 2020.

[41] Ghate, A. S., Kenway, G., Stich, G.-D., Browne, O., Housman, J., and Kiris, C. C., "Transonic lift and drag predictions using Wall-Modelled Large Eddy Simulations," *AIAA Scitech 2021 FORUM*, 2021.

[42] Brehm, C., Barad, M., Housman, J., and Kiris, C., "A Comparison of Higher-Order Finite-Difference Shock Capturing Schemes," *Computers & Fluids*, Vol. 122, 2015, pp. 184–208.

[43] Shu, C.-W., "High Order Weighted Essentially Nonoscillatory Schemes for Convection Dominated Problems," *SIAM Review*, Vol. 51, No. 1, 2009, pp. 92–126.

[44] Deng, X., and H., Z., "Developing High-Order Weighted Compact Nonlinear Schemes," *Journal of Computational Physics*, Vol. 165, 2000, pp. 22–44.

[45] Wong, M. L., and Lele, S. K., "High-order localized dissipation weighted compact nonlinear scheme for shock-and interface-capturing in compressible flows," *Journal of Computational Physics*, Vol. 339, 2017, pp. 179–209.

[46] Wong, M. L., Angel, J. B., Barad, M. F., and Kiris, C. C., "A positivity-preserving high-order weighted compact nonlinear scheme for compressible gas-liquid flows," *Journal of Computational Physics*, Vol. 444, 2021, p. 110569.

[47] Deng, X., Mao, M., Jiang, Y., and Liu, H., "New High-Order Hybrid Cell-Edge and Cell-Node Weighted Compact Nonlinear Schemes," *20th AIAA Computational Fluid Dynamics Conference, Honolulu, Hawaii*, 2011. AIAA-2011-3857.

[48] Housman, J., Kiris, C., and Hafez, M., "Preconditioned methods for simulations of low speed compressible flows," *Computers & Fluids*, Vol. 38, No. 7, 2009, pp. 1411–1423.

[49] Deng, X., Mao, M., Tu, G., Liu, H., and Zhang, H., "Geometric Conservation Law and Applications to High-Order Finite Difference Schemes with Stationary Grids," *Journal of Computational Physics*, Vol. 230, 2011, pp. 1100–1115.

[50] Nonomura, T., and Fujii, K., "Robust Explicit Formulation of Weighted Compact Nonlinear Scheme," *Computers & Fluids*, Vol. 85, 2013, pp. 8–18.

[51] Thornber, B., Mosedale, A., Drikakis, D., Youngs, D., and Williams, R. J., "An improved reconstruction method for compressible flow with low Mach number features," *Theoretical and Computational Fluid Dynamics*, Vol. 26, 2012, pp. 523–550.

[52] Housman, J., and Kiris, C., "Slat Noise Predictions using Higher-Order Finite-Difference Methods on Overset Grids," *22nd AIAA/CEAS Aeroacoustic Conference, Lyon, France*, 2016. AIAA-2016-2963.

[53] Musker, A., "Explicit expression for the smooth wall velocity distribution in a turbulent boundary layer," *AIAA Journal*, Vol. 17, No. 6, 1979, pp. 655–657.

[54] Bocquet, S., Sagaut, P., and Jouhaud, J., "A compressible wall model for large-eddy simulation with application to prediction of aerothermal quantities," *Physics of fluids*, Vol. 24, No. 6, 2012, p. 065103.

[55] Larsson, J., Kawai, S., Bodart, J., and Bermejo-Moreno, I., "Large eddy simulation with modeled wall-stress: recent progress and future directions," *Mechanical Engineering Reviews*, Vol. 3, No. 1, 2016, pp. 15–00418.

[56] Vreman, A., "An eddy-viscosity subgrid-scale model for turbulent shear flow: Algebraic theory and applications," *Physics of fluids*, Vol. 16, No. 10, 2004, pp. 3670–3681.

[57] Bose, S. T., and Park, G. I., "Wall-modeled large-eddy simulation for complex turbulent flows," *Annual review of fluid mechanics*, Vol. 50, 2018, pp. 535–561.

[58] Kiris, C., Ghate, A., Duensing, J., Browne, O., Housman, J., Stich, G., Kenway, G., Fernandez, and L. Machado, L., "High-Lift Common Research Model: RANS, HRLES, and WMLES perspectives for CLmax prediction using LAVA." *AIAA SCITECH 2022 FORUM*, 2022.

[59] Bres, G., Nichols, J., Lele, S., and Ham, F., "Large Eddy Simulation for Jet Noise: the Importance of Getting the Boundary Layer Right," *21st AIAA/CEAS Aeroacoustics Conference, Dallas, Texas*, 2015. AIAA-2015-2535.

[60] Uzun, A., and Hussaini, M. Y., "Investigation of High Frequency Noise Generation in the Near-Nozzle Region of a Jet Using Large Eddy Simulation," *Theoretical and Computational Fluid Dynamics*, Vol. 21, 2007, pp. 291–321.

[61] Aikens, K., Blaisdell, G., and Lyrintzis, A., "Analysis of Converging-Diverging Beveled Nozzle Jets Using Large Eddy Simulation with a Wall Model," *53rd AIAA Aerospace Sciences Meeting, Kissimmee, Florida*, 2015. AIAA-2015-0509.

[62] Jarrin, N., Benhamadouche, S., Laurence, D., and Prosser, R., "A Synthetic-Eddy-Method for Generating Inflow Conditions for Large-Eddy Simulations," *International Journal of Heat and Fluid Flow*, Vol. 27, 2006, pp. 585–593.

[63] Jarrin, N., Prosser, R., Uribe, J.-C., Benhamadouche, S., and Laurence, D., "Reconstruction of Turbulent Fluctuations for Hybrid RANS/LES simulations using a Synthetic-Eddy Method," *International Journal of Heat and Fluid Flow*, Vol. 30, 2009, pp. 435–442.

[64] Bogey, C., and Marsden, O., "A Study of the Grid Dependence of the Flow Field and Noise of Subsonic Jets," *54th AIAA Aerospace Science Meeting, San Diego, Ca*, 2016. AIAA-2016-0261.

[65] Mendez, S., Shoeybi, M., Lele, S., and Moin, P., "On the use of the Ffowcs Williams-Hawkings Equation to Predict Far-Field Jet Noise from Large Eddy-Simulations," *International Journal of Aeroacoustics*, Vol. 12, 2013.

[66] Slotnick, J., "CFD Vision 2030 Study: A Path to Revolutionary Computational Aerosciences," *NASA Technical Report*, 2014. NASA/CR-2014-218178.

[67] Bogey, C., Bailly, C., and Juve, D., "Investigation of Downstream and Sideline Subsoniuc Jet Noise Using Large Eddy Simulation," *Theor. Comput. Fluid Dyn.*, Vol. 20, 2006, pp. 23–40.

[68] Bogey, C., and Bailly, C., "Influence of nozzle-exit boundary-layer conditions on the flow and acoustic fields of initialllz laminar jets," *Journal of Fluid Mechanics*, Vol. 10, 2010, pp. 507–538.

[69] Mendez, S., Shoeybi, M., Sharma, A., Ham, F., Lele, S., and Moin, P., "Large-Eddy Simulations of Perfectly-Expanded Supersonics Jets: Quality Assessment and Validation," *48th AIAA Aerospace Sciences Meeting, Orlando, Florida*, 2010. AIAA-2010-271.

[70] Rahier, G., Prieru, J., Vuillot, F., and Biancherin, A., "Investigation of integral surface formulations of acoustic predictions of hot jets starting from unsteady aerodynamic simulations," 2003. AIAA-2003-3164.

[71] Shur, M., Spalart, P. R., and Strelets, M., "Noise prediction for increasingly complex jets, Part 1 Methods and Tests," *International Journal of Aeroacoustics*, Vol. 4, 2005, pp. 213–246.

[72] Shur, M., Spalart, P. R., and Strelets, M., "Noise prediction for increasingly complex jets, Part 2 Applications," *International Journal of Aeroacoustics*, Vol. 4, 2005, pp. 247–266.

[73] Lockard, D., "A Comparison of Ffowcs Williams-Hawkings Solvers for Airframe Noise Applications," *8th AIAA/CEAS Aeroacoustics Conference & Exhibit, Breckenridge, Colorado*, 2002. AIAA-2002-2580.

[74] Spalart, P. R., and Shur, M., "Variants of the Ffowcs Williams-Hawkings Equation and their Coupling with Simulations of Hot Jets," *International Journal of Aeroacoutics*, Vol. 8, No. 5, 2009, pp. 477–492.

[75] Ghate, A., Towne, A., and Lele, S., "Broadband reconstruction of inhomogeneous turbulence using spectral proper orthogonal decomposition and Gabor modes," *Journal of Fluid Mechanics*, Vol. 888, 2020.

[76] Ghate, A. S., and Lele, S. K., "Gabor mode enrichment in large eddy simulations of turbulent flow," *Journal of Fluid Mechanics*, Vol. 903, 2020, p. A13. https://doi.org/10.1017/jfm.2020.622.

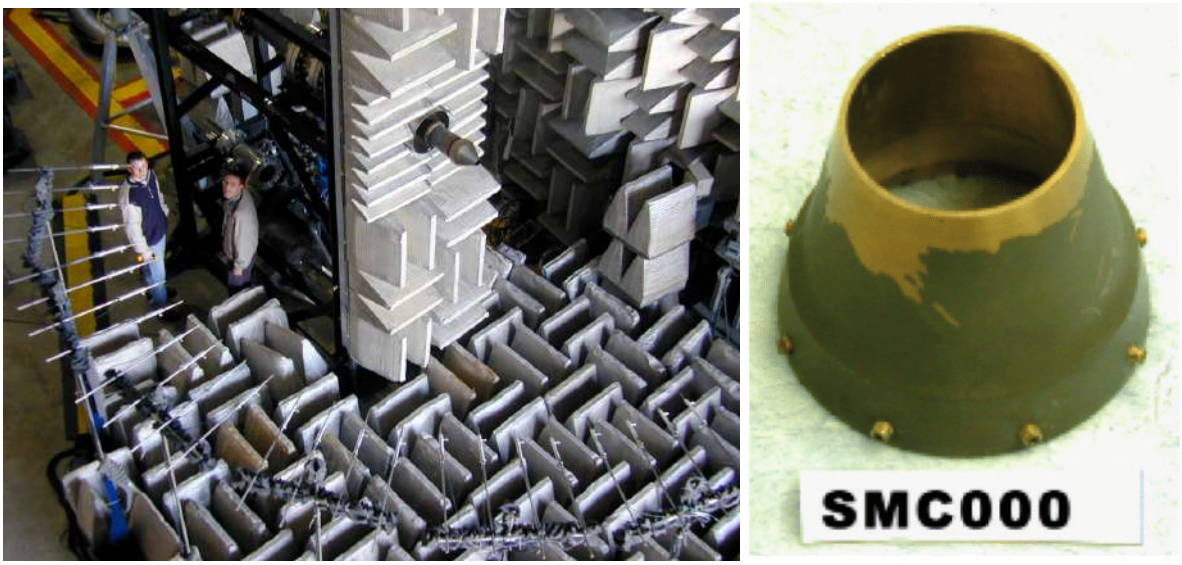

(a) SHAR (b) SMC000 round jet

Fig. 1 (a) Picture of the Small Hot Jet Acoustic Rig (SHJAR) in acoustic configuration with 24 microphones centered around the nozzle exit [8]. (b) SMC000 single stream nozzle used in this study. Drill holes for mounting the nozzle have not been considered in the CFD simulation to simplify the meshing. The nozzle has an exit diameter of 2 inch.

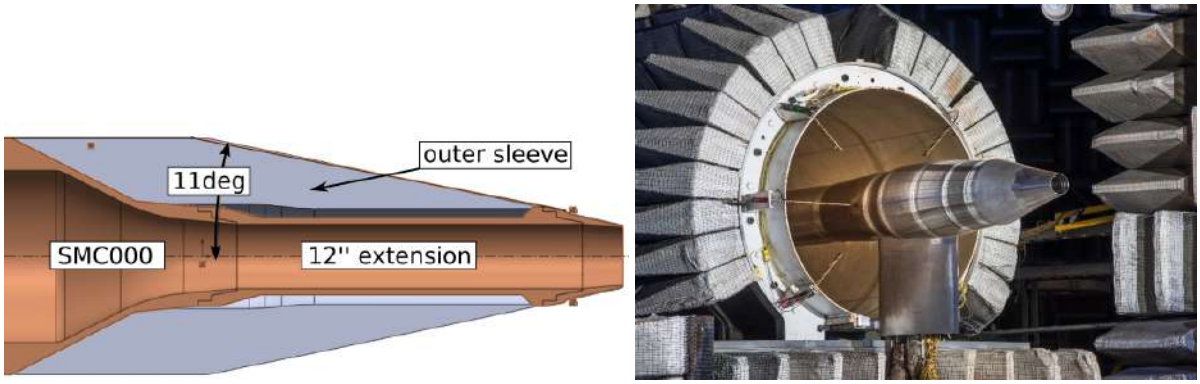

(a) (b)

Fig. 2 (a) Sketch of geometric change to SMC000 2 inch nozzle to account for in-flight configuration with outer sleeve consistent with NATAR C4-S1-P1 + ext configuration displayed in (b).

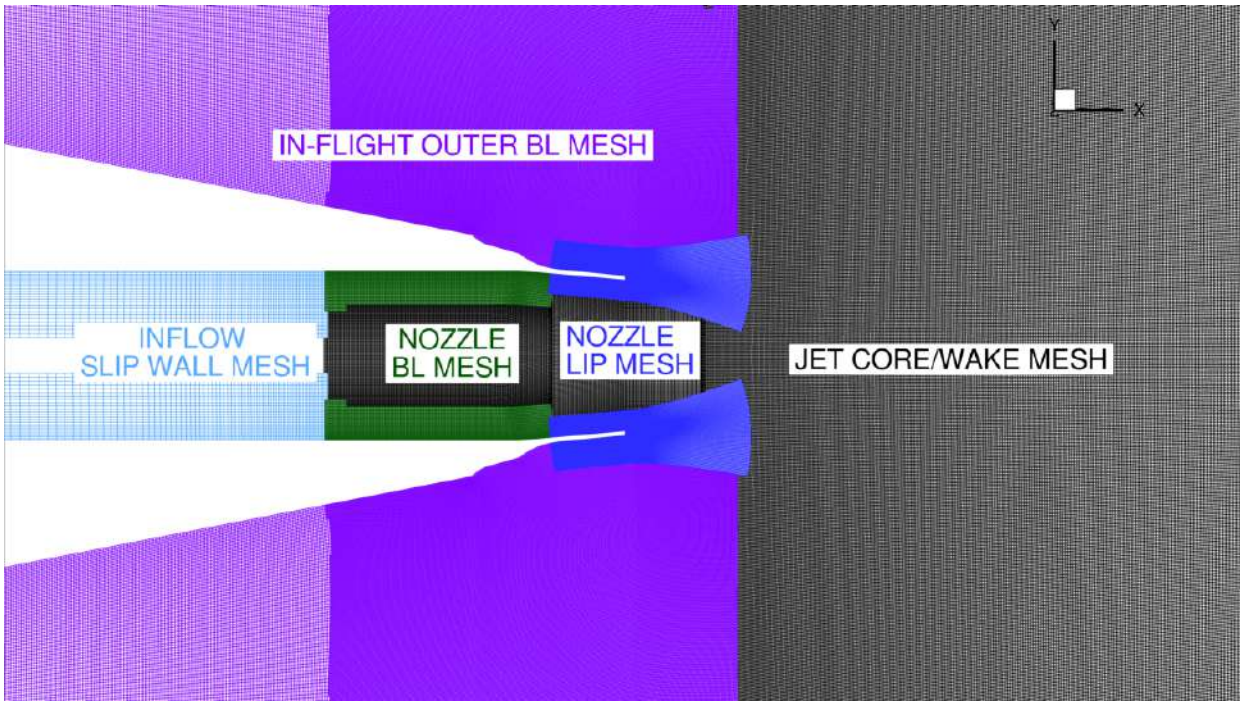

Fig. 3 Depiction of five different meshing regions described in section IV.

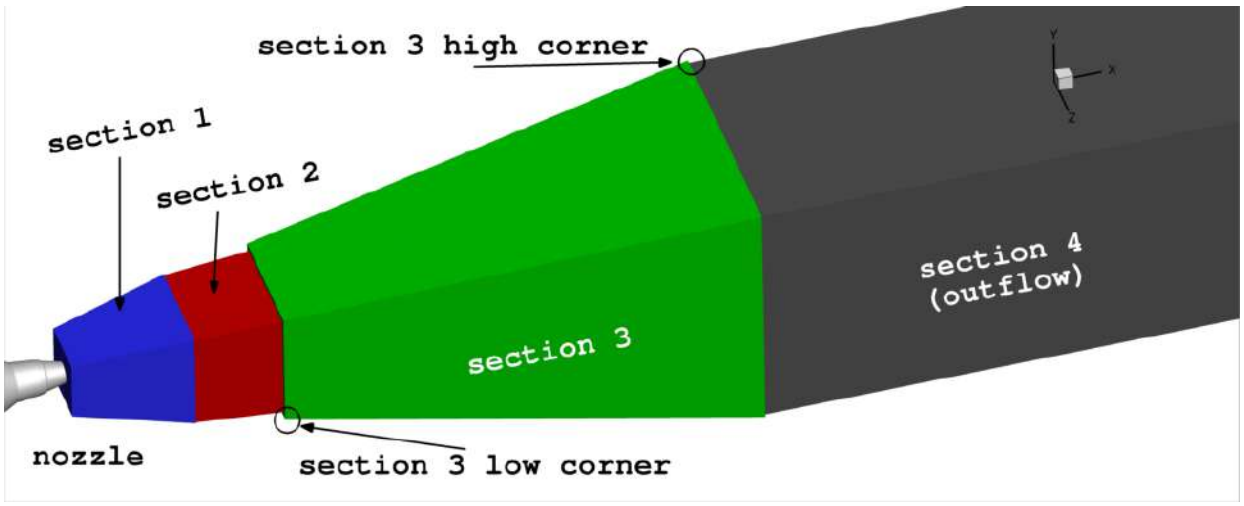

Fig. 4 Outline of nozzle wake mesh refinement. Spacings for each section can be seen in table 2.

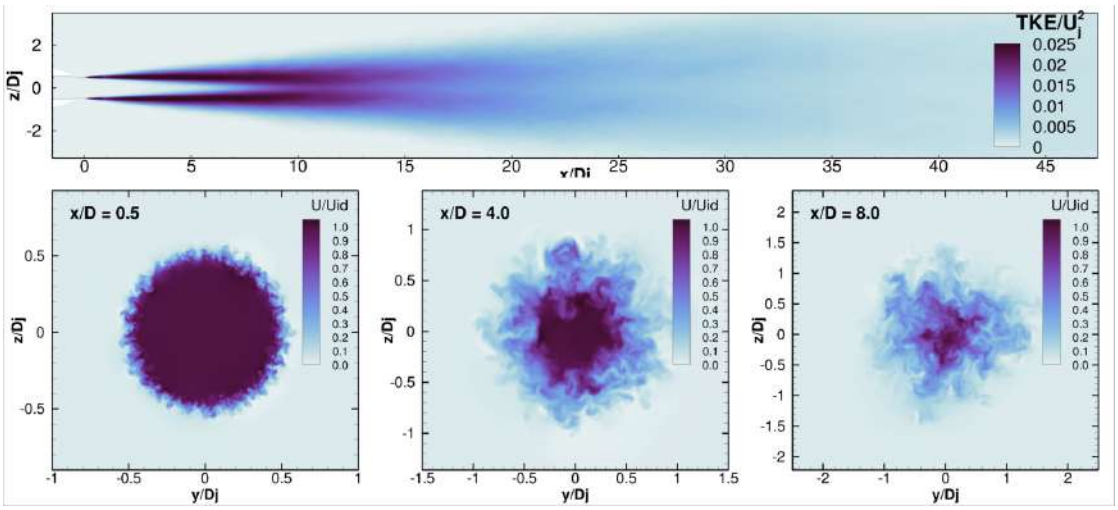

(a) SP3: Ma = 0.50 ; NPR = 1.197 ; NTR = 0.96

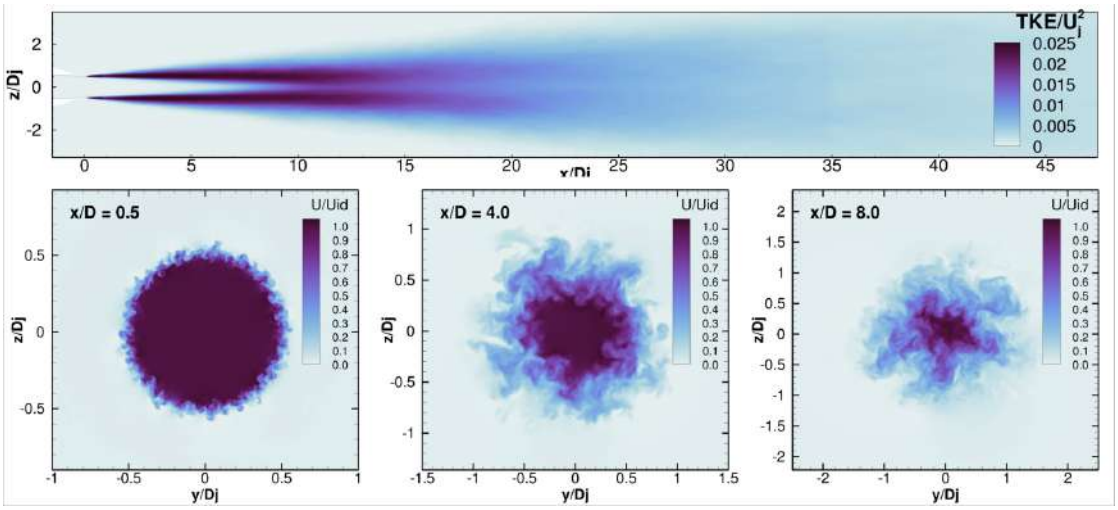

(b) SP7: Ma = 0.90 ; NPR = 1.852 ; NTR = 0.84

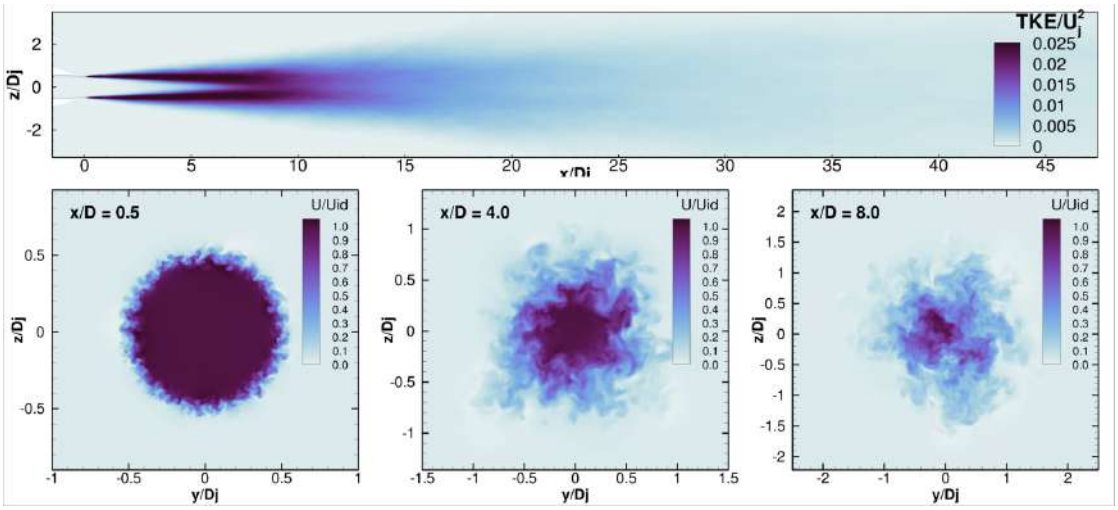

(c) SP23: Ma = 0.90 ; NPR = 1.852 ; NTR = 0.84

Fig. 5 Instantaneous streamwise velocity normalized by jet exit centerline velocity at x/D=0.5,4.0,8.0. Turbulent kinetic energy at y/D=0.0.

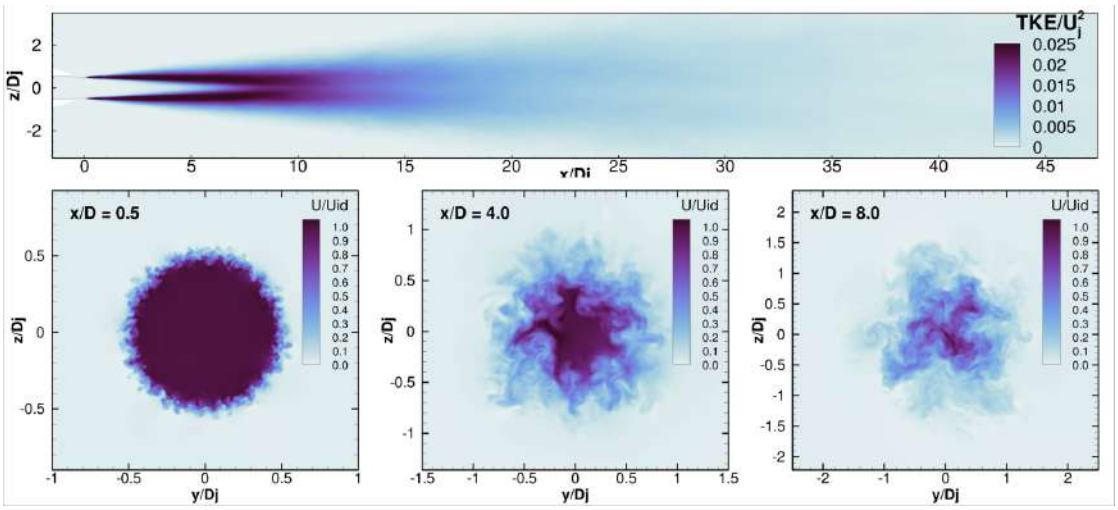

(a) SP27: Ma = 0.90 ; NPR = 1.368 ; NTR = 1.76

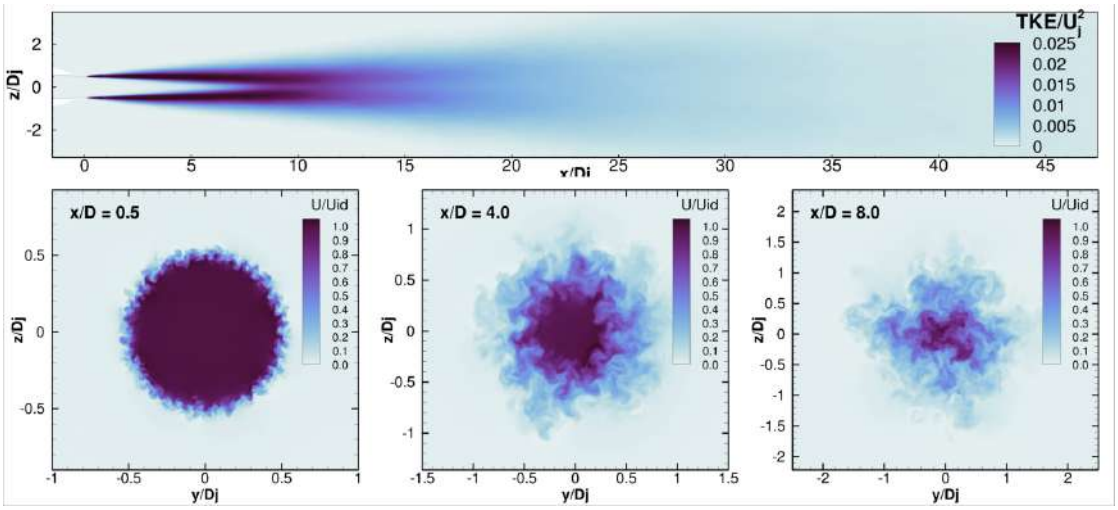

(b) SP29: Ma = 1.33 ; NPR = 1.898 ; NTR = 1.76

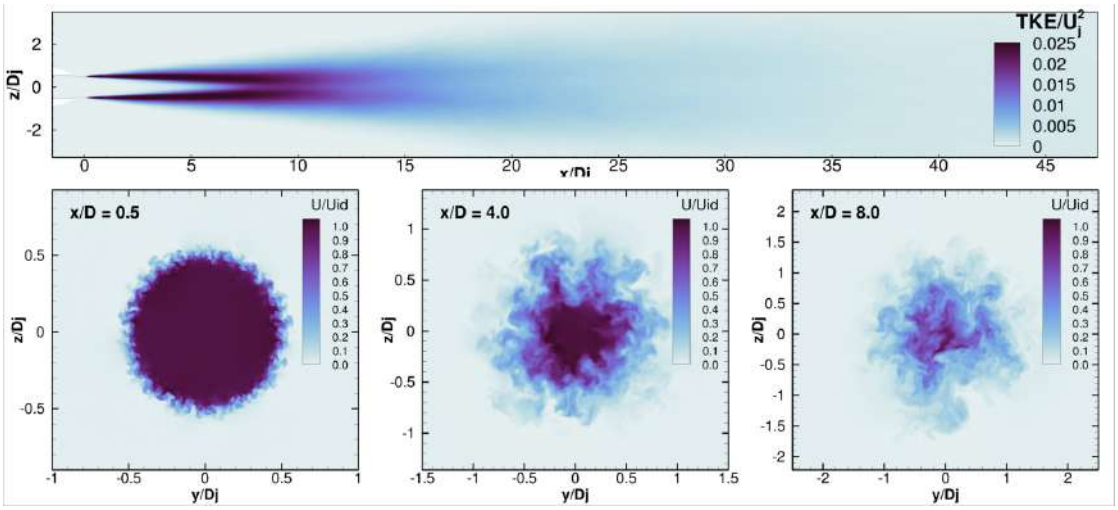

(c) SP38: Ma = 1.33 ; NPR = 1.664 ; NTR = 2.27

Fig. 6 Instantaneous streamwise velocity normalized by jet exit centerline velocity at x/D=0.5,4.0,8.0. Turbulent kinetic energy at y/D=0.0.

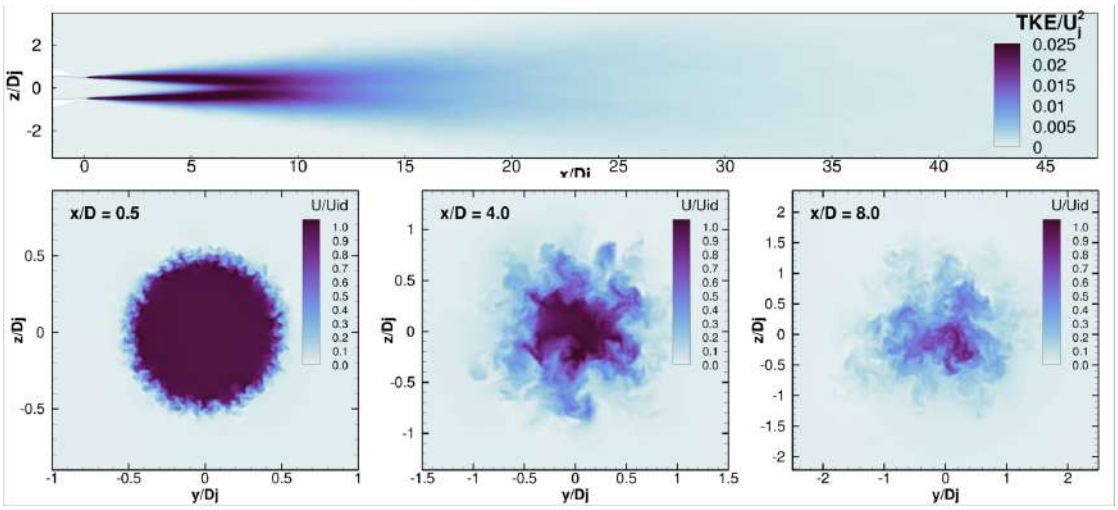

(a) SP46: Ma = 0.9 ; NPR = 1.219 ; NTR = 2.70

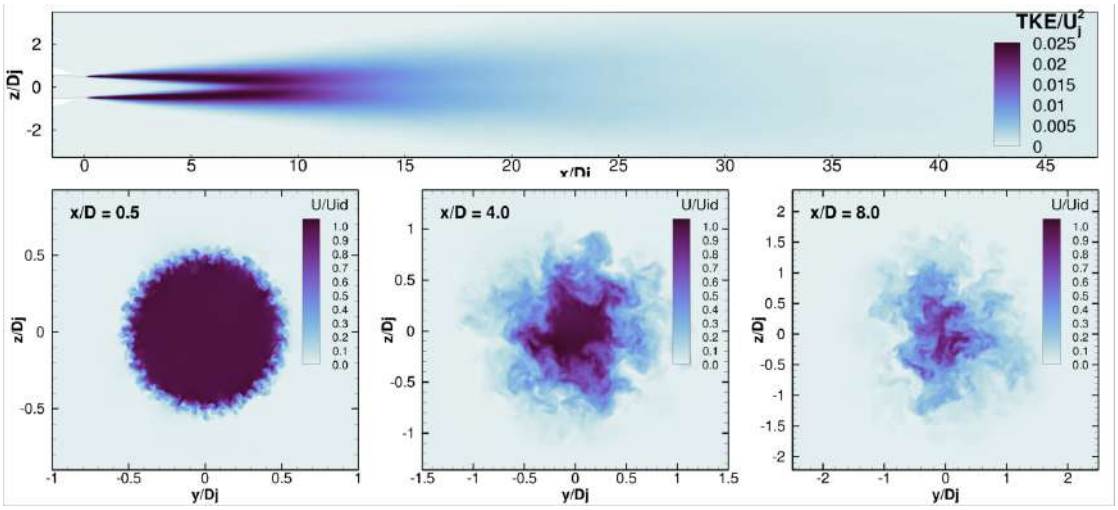

(b) SP49: Ma = 1.48 ; NPR = 1.697 ; NTR = 2.70

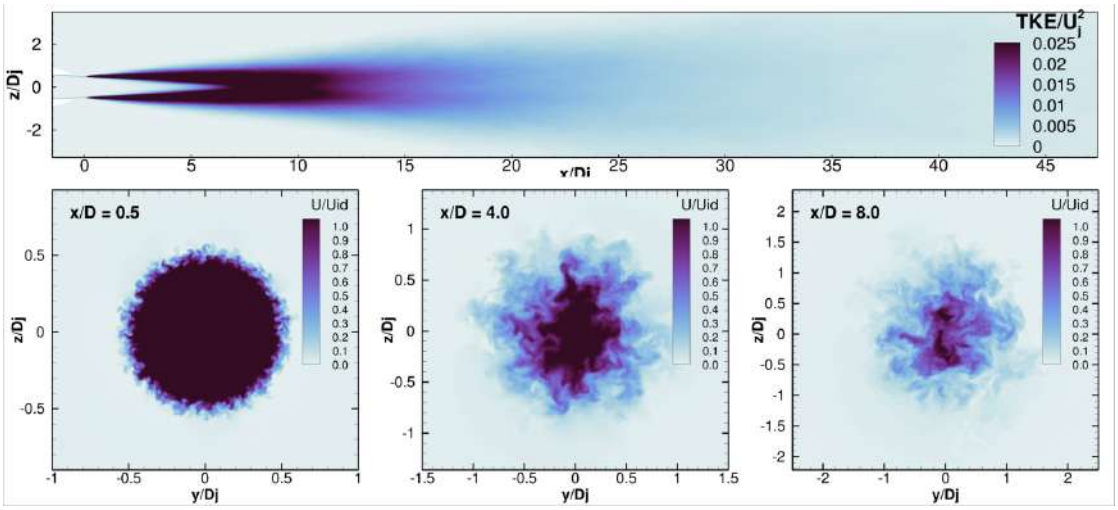

(c) SP101240: Ma = 1.14 ; NPR = 1.608 ; NTR = 2.78

Fig. 7 Instantaneous streamwise velocity normalized by jet exit centerline velocity at x/D=0.5,4.0,8.0. Turbulent kinetic energy at y/D=0.0.

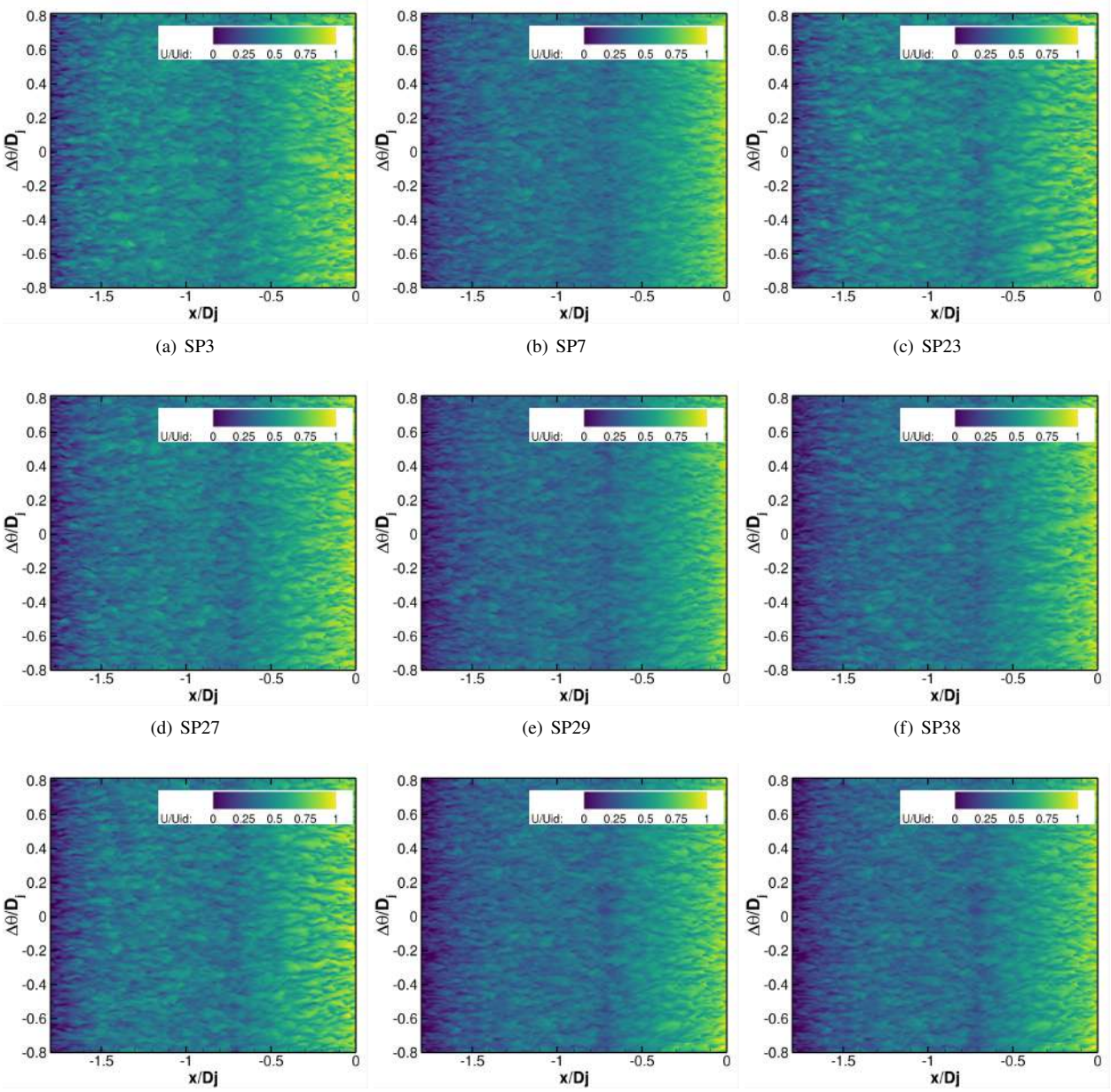

(a) SP3 (b) SP7 (c) SP23

(d) SP27 (e) SP29 (f) SP38

(g) SP46 (h) SP49 (i) SP101240

Fig. 8 Zoom-in view of instantaneous flow field inside of nozzle. Wall-normal velocity displayed at a constant distance of $2\Delta x$ from the nozzle surface (unrolled).

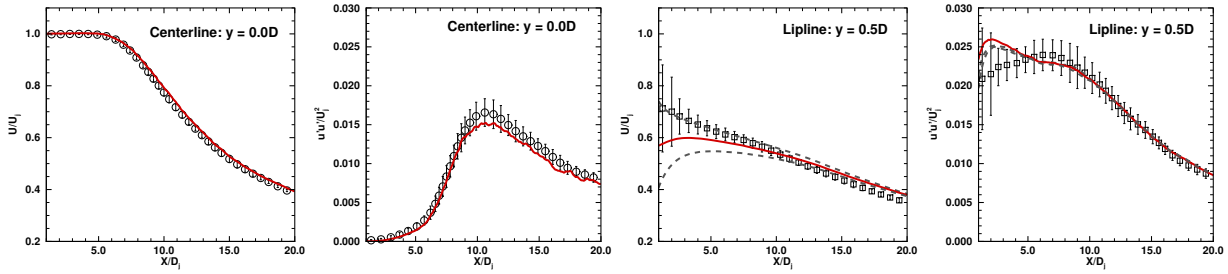

(a) SP3: Ma = 0.50 ; NPR = 1.197 ; NTR = 0.96

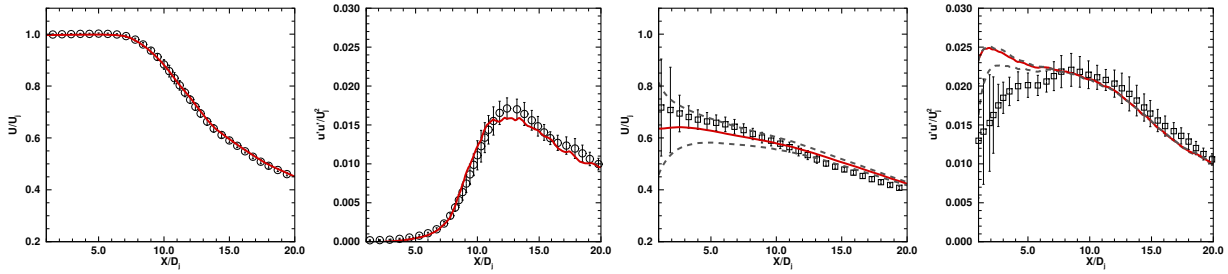

(b) SP7: Ma = 0.90 ; NPR = 1.852 ; NTR = 0.84

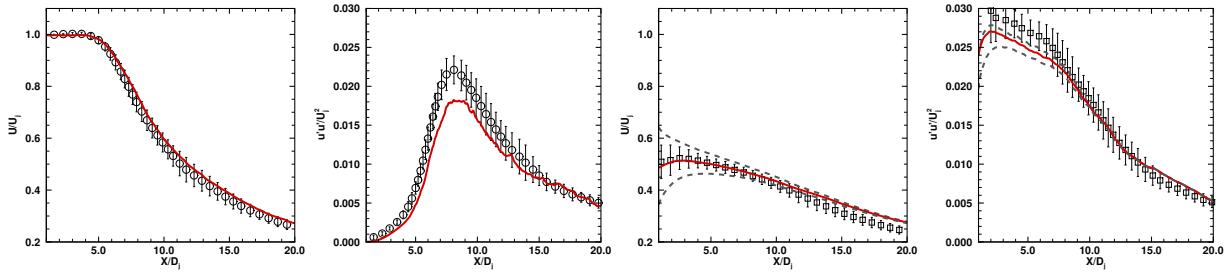

(c) SP23: Ma = 0.90 ; NPR = 1.852 ; NTR = 0.84

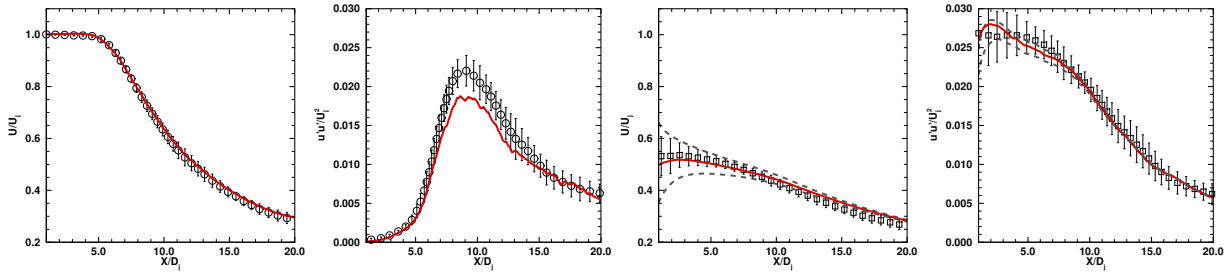

(d) SP27: Ma = 0.90 ; NPR = 1.368 ; NTR = 1.76

Fig. 9 Time-averaged centerline (circle) and lipline (square) velocity and normal-stress compared with experiments by Bridges *et al.*. The grey dashed lines represent data taken at a constant distance of 0.01D above and below the lipline.

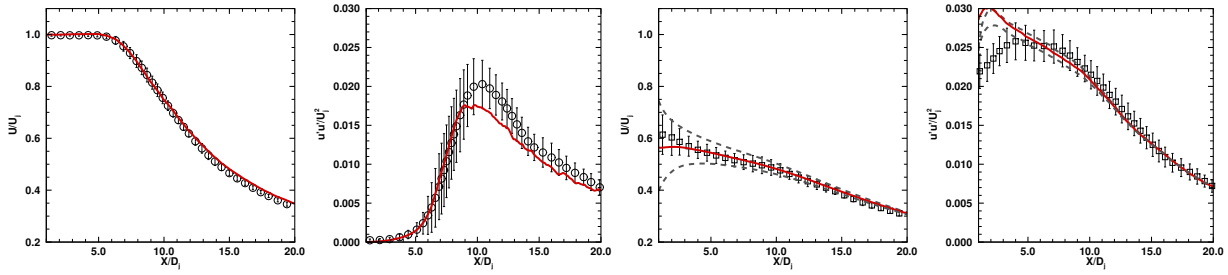

(a) SP29: Ma = 1.33 ; NPR = 1.898 ; NTR = 1.76

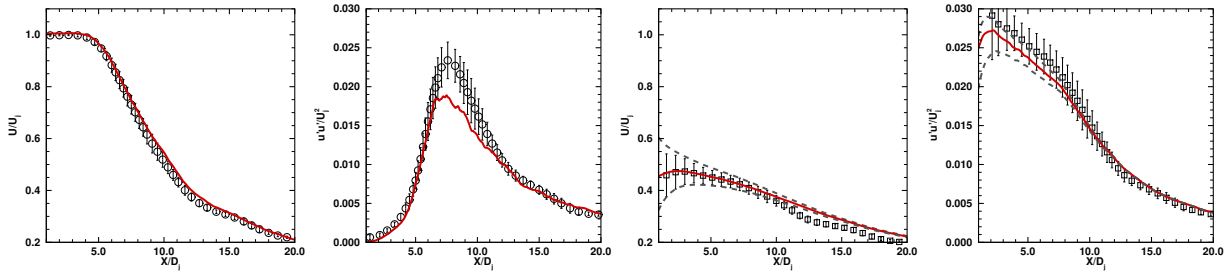

(b) SP46: Ma = 0.9 ; NPR = 1.219 ; NTR = 2.70

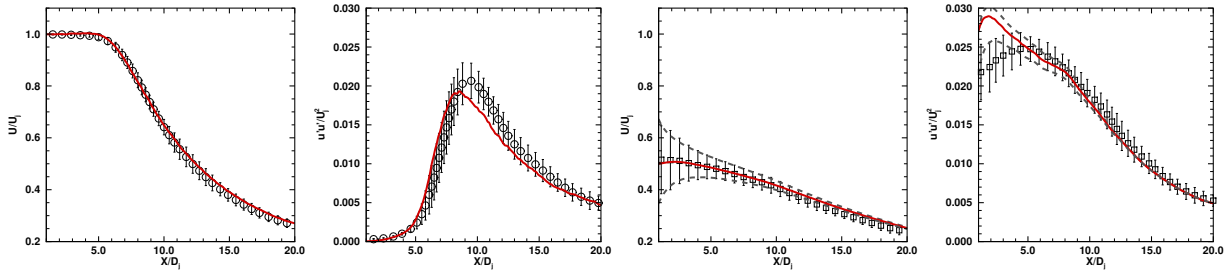

(c) SP49: Ma = 1.48 ; NPR = 1.697 ; NTR = 2.70

Fig. 10 Time-averaged centerline (circle) and lipline (square) velocity and normal-stress compared with experiments by Bridges *et al.*. The grey dashed lines represent data taken at a constant distance of 0.01D above and below the lipline.

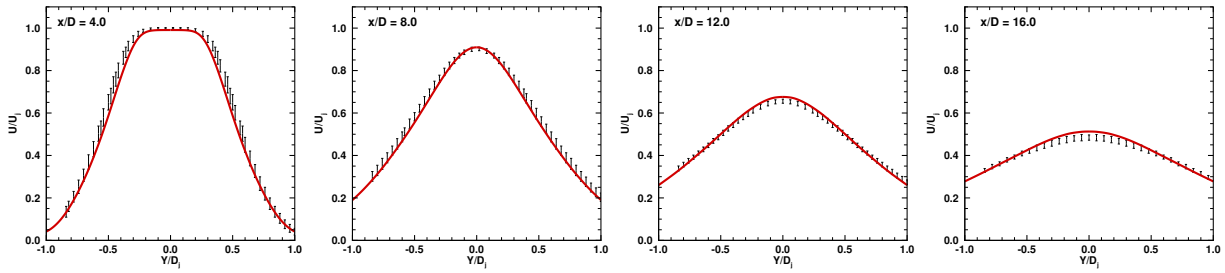

(a) SP3: Ma = 0.50 ; NPR = 1.197 ; NTR = 0.96

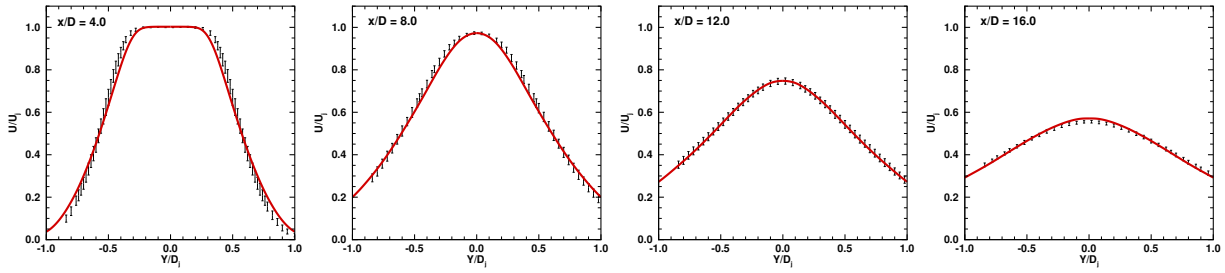

(b) SP7: Ma = 0.90 ; NPR = 1.852 ; NTR = 0.84

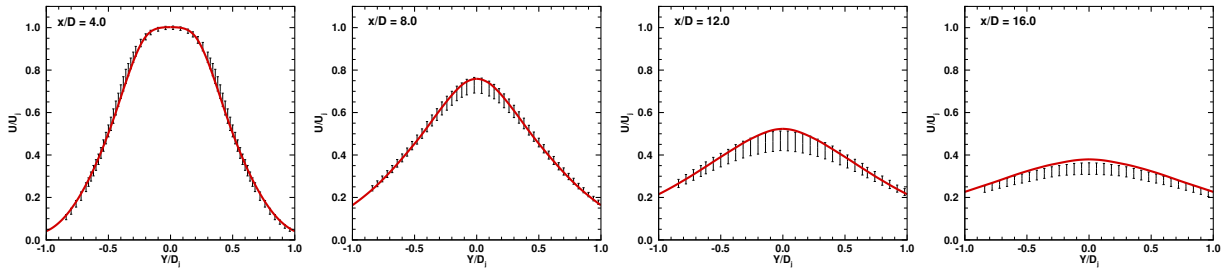

(c) SP23: Ma = 0.50 ; NPR = 1.852 ; NTR = 1.76

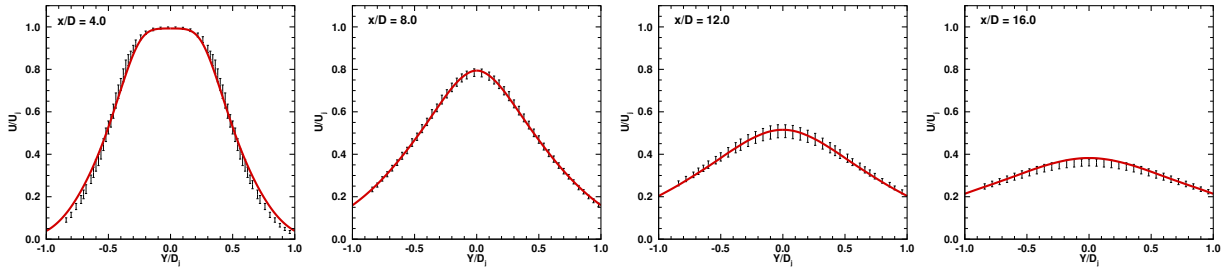

(d) SP27: Ma = 0.90 ; NPR = 1.368 ; NTR = 1.76

Fig. 11 Comparison of time-averaged axial velocity with experiments by Bridges *et al.*. Normalization with centerline velocity U_{jet} and nozzle exit diameter D_{jet}.

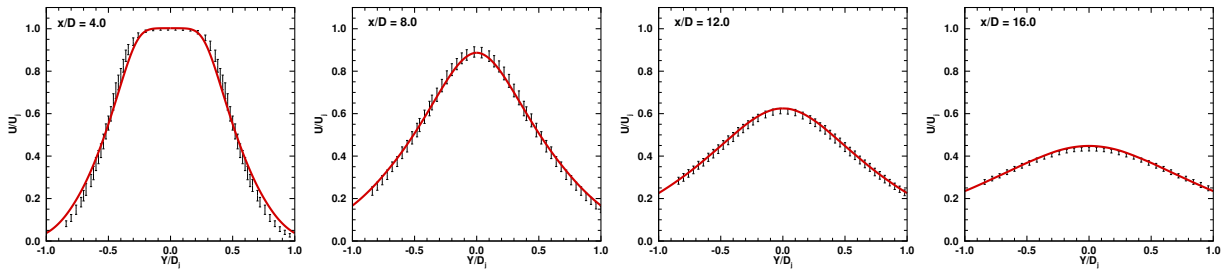

(a) SP29: Ma = 1.33 ; NPR = 1.898 ; NTR = 1.76

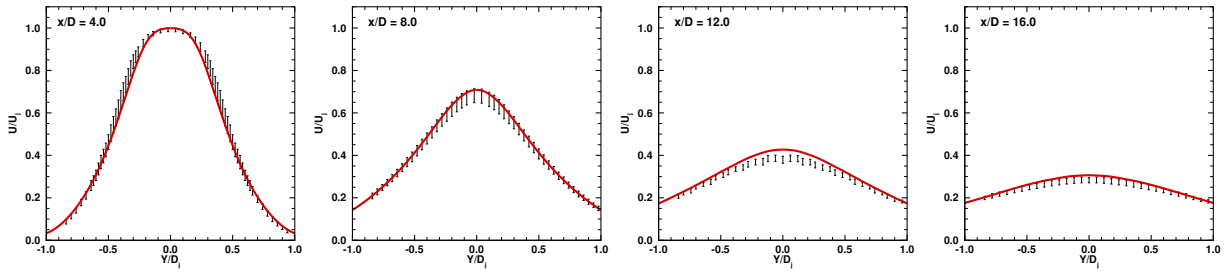

(b) SP46: Ma = 0.9 ; NPR = 1.219 ; NTR = 2.70

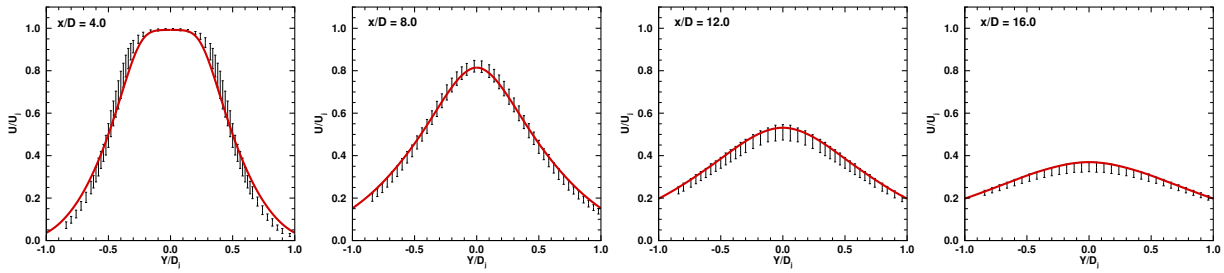

(c) SP49: Ma = 1.48 ; NPR = 1.697 ; NTR = 2.70

Fig. 12 Comparison of time-averaged axial velocity with experiments by Bridges *et al.*. Normalization with centerline velocity U_{jet} and nozzle exit diameter D_{jet}.

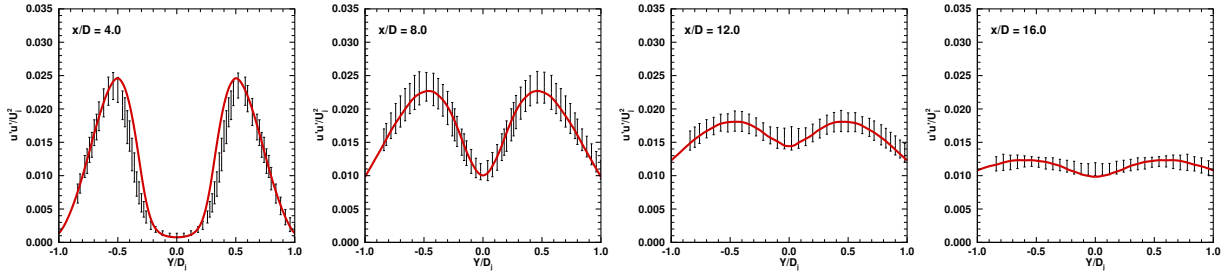

(a) SP3: Ma = 0.50 ; NPR = 1.197 ; NTR = 0.96

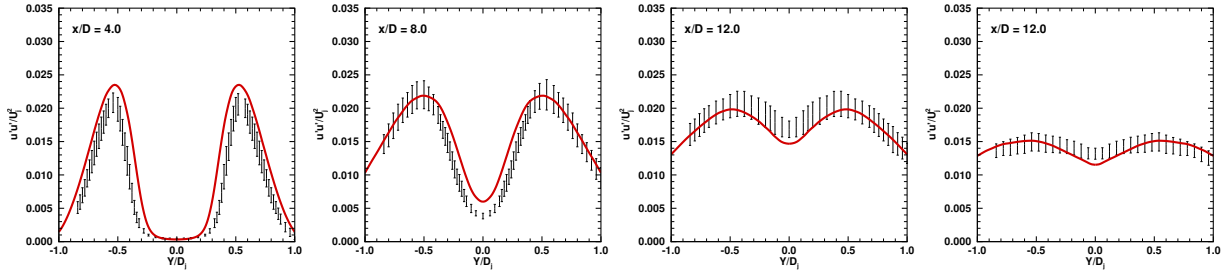

(b) SP7: Ma = 0.90 ; NPR = 1.852 ; NTR = 0.84

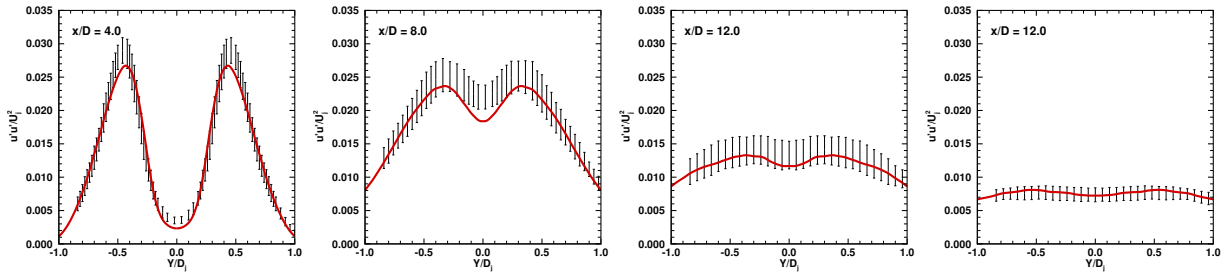

(c) SP23: Ma = 0.50 ; NPR = 1.852 ; NTR = 1.76

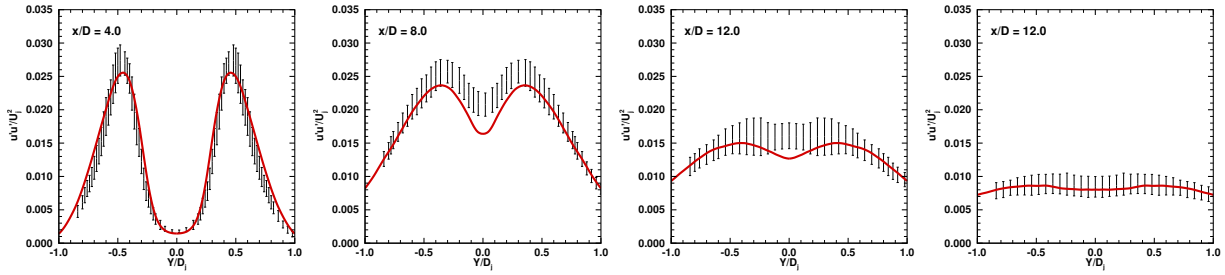

(d) SP27: Ma = 0.90 ; NPR = 1.368 ; NTR = 1.76

Fig. 13 Comparison of time-averaged axial normal stress with experiments by Bridges *et al.*. Normalization with centerline velocity U_{jet} and nozzle exit diameter D_{jet}.

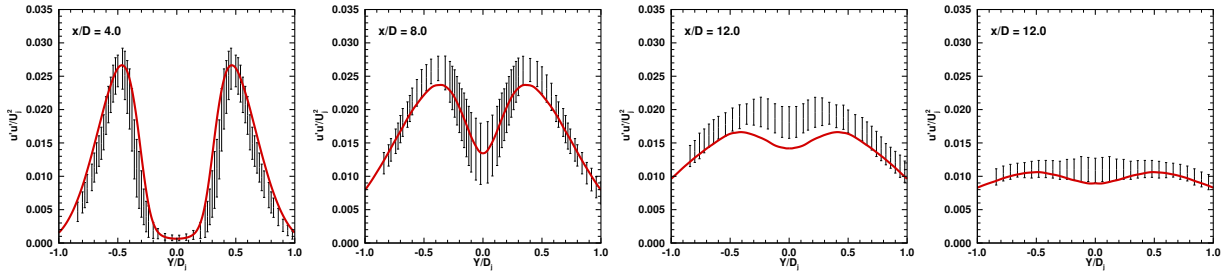

(a) SP29: Ma = 1.33 ; NPR = 1.898 ; NTR = 1.76

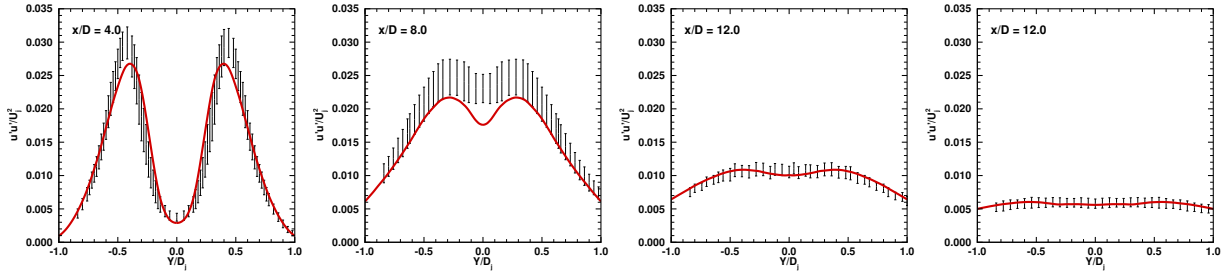

(b) SP46: Ma = 0.9 ; NPR = 1.219 ; NTR = 2.70

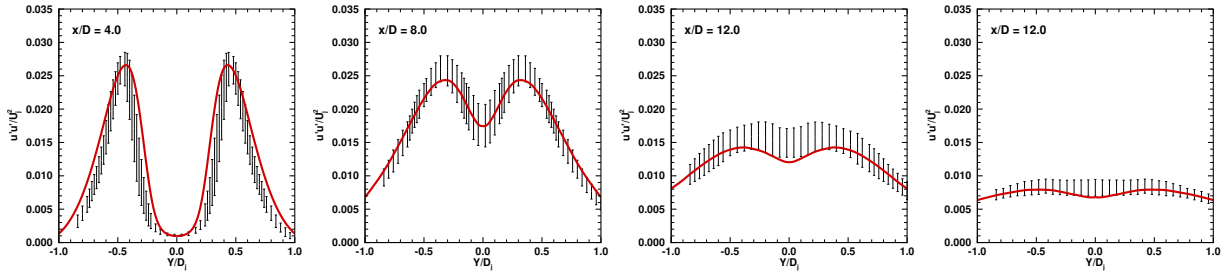

(c) SP49: Ma = 1.48 ; NPR = 1.697 ; NTR = 2.70

Fig. 14 Comparison of time-averaged axial normal stress with experiments by Bridges *et al.*. Normalization with centerline velocity U_{jet} and nozzle exit diameter D_{jet}.

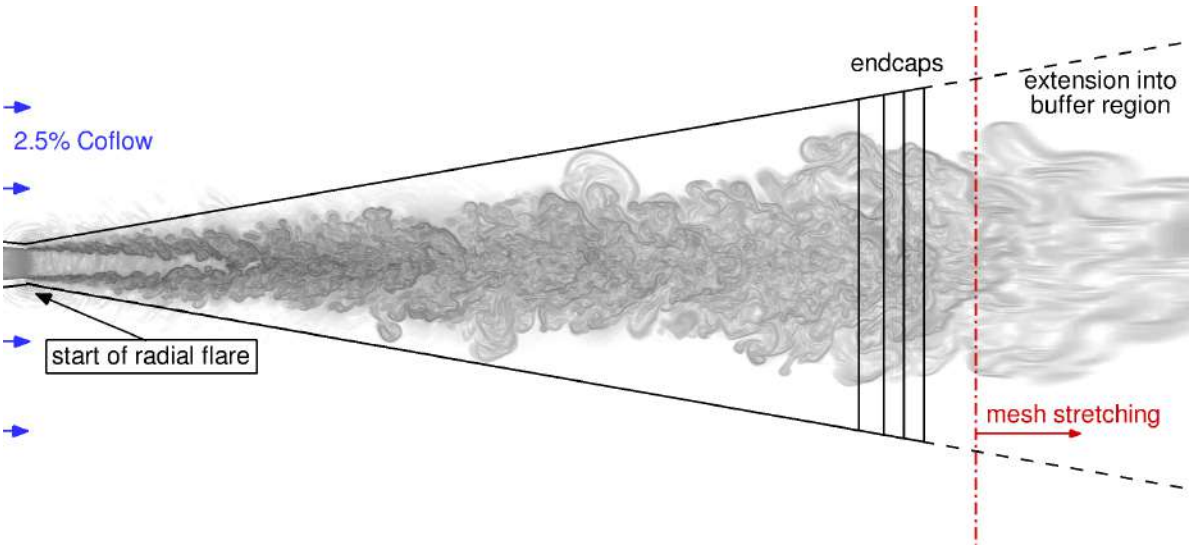

Fig. 15 Outline of FWH surface placement with end-caps between 25D and 30D (solid line) and open outflow disk FWH surface extended into the outflow buffer region (dashed line). Density gradient of magnitude displayed on the centerline plane for the fine CFD mesh. (Number of end-caps has been reduced from 25 to 4 in this sketch for displaying purposes)

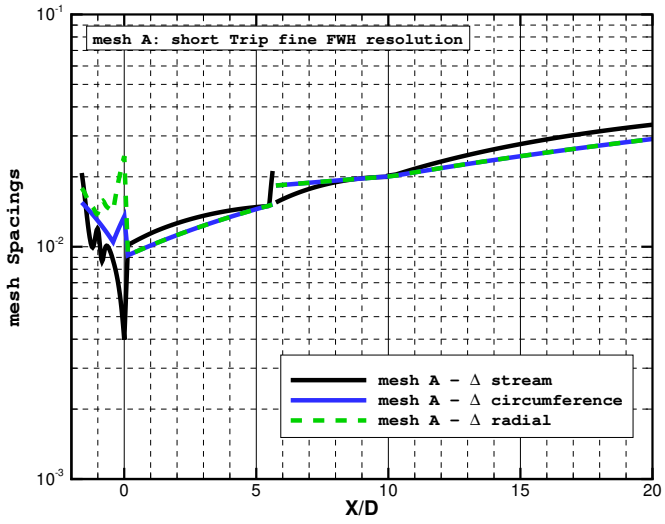

(a) mesh-A and mesh-B (fine)

Fig. 16 Dimensionless mesh spacing of underlying CFD grid along the conical FWH surface triangulation, in streamwise direction $\Delta x/D$ (black solid), azimuthal $\Delta\Theta/D$ (blue solid), radial $\Delta r/D$ (green dashed) and maximum aspect ratio $max\Delta/min\Delta$ (red solid).

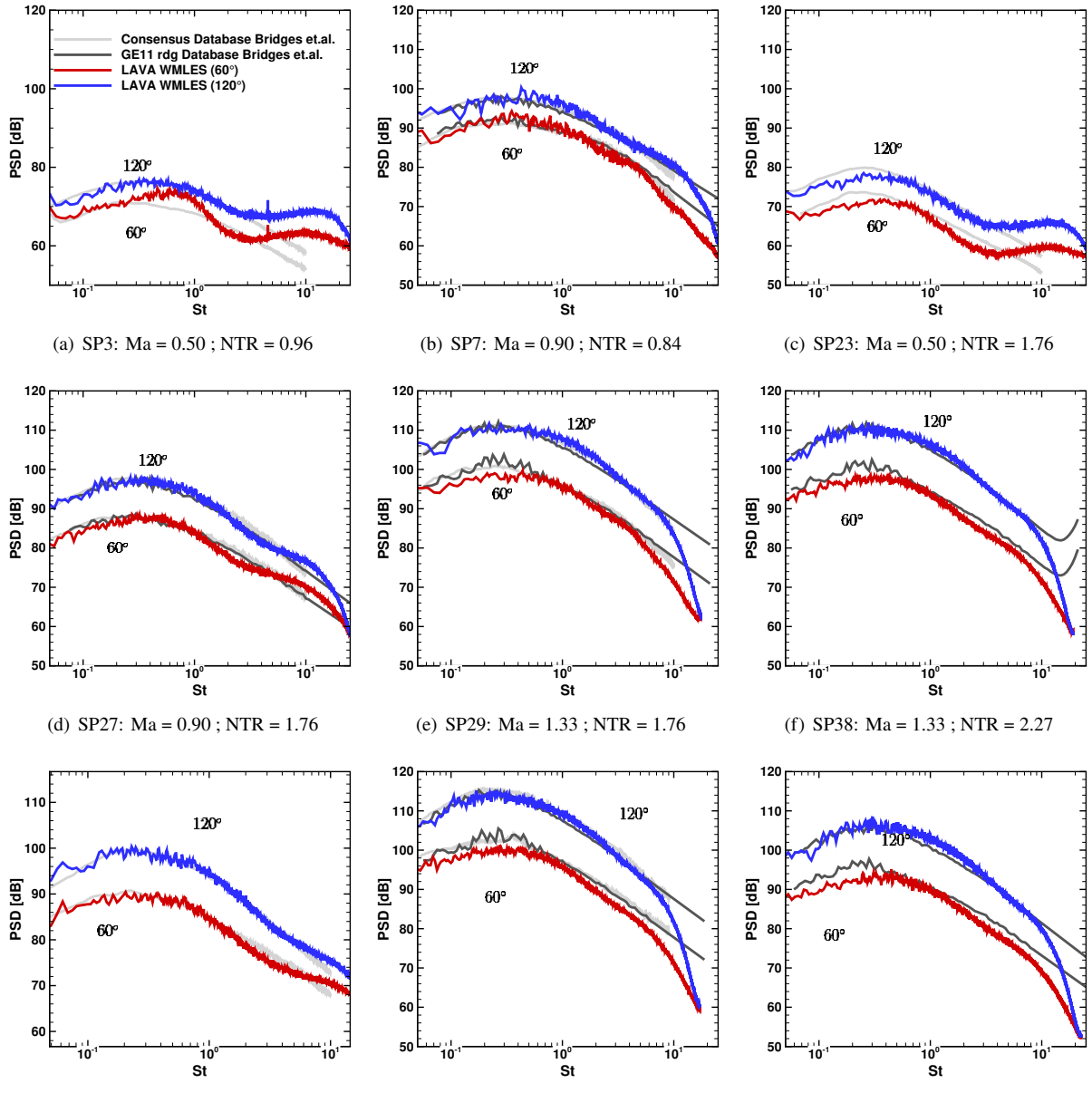

(a) SP3: Ma = 0.50 ; NTR = 0.96

(b) SP7: Ma = 0.90 ; NTR = 0.84

(c) SP23: Ma = 0.50 ; NTR = 1.76

(d) SP27: Ma = 0.90 ; NTR = 1.76

(e) SP29: Ma = 1.33 ; NTR = 1.76

(f) SP38: Ma = 1.33 ; NTR = 2.27

(g) SP46: Ma = 0.90 ; NTR = 2.70

(h) SP49: Ma = 1.48 ; NTR = 2.70

(i) SP101240: Ma = 1.14 ; NTR = 1.78

Fig. 17 Comparison of noise spectra obtained from LAVA-WMLES simulations with experiments by Bridges *et al.*. All simulations use a consistent FWH surface triangulation. Averaging over 72 observers in azimuth is applied for each polar angle at 60 deg (red) and 120 deg (blue).

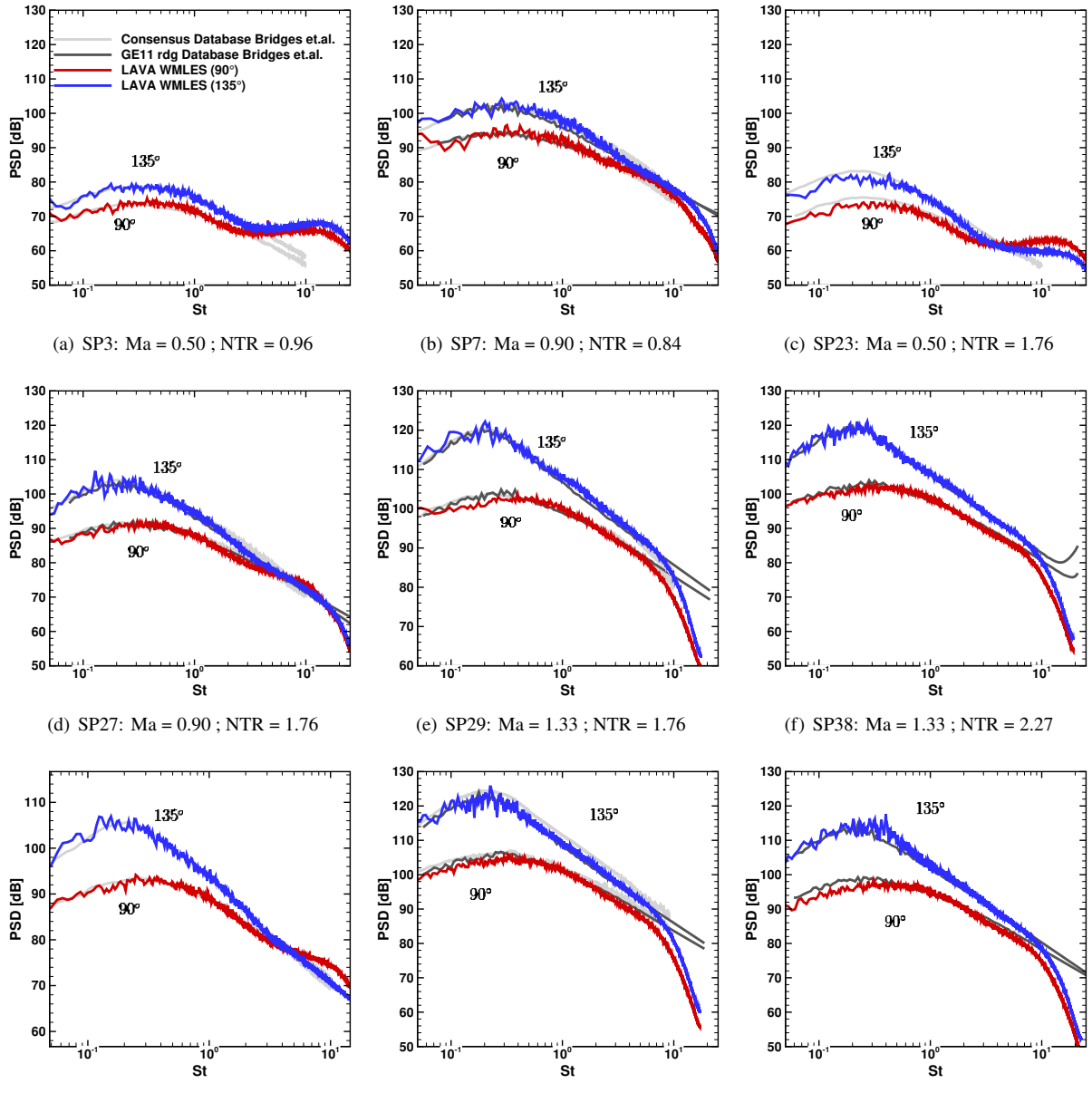

(a) SP3: Ma = 0.50 ; NTR = 0.96

(b) SP7: Ma = 0.90 ; NTR = 0.84

(c) SP23: Ma = 0.50 ; NTR = 1.76

(d) SP27: Ma = 0.90 ; NTR = 1.76

(e) SP29: Ma = 1.33 ; NTR = 1.76

(f) SP38: Ma = 1.33 ; NTR = 2.27

(g) SP46: Ma = 0.90 ; NTR = 2.70

(h) SP49: Ma = 1.48 ; NTR = 2.70

(i) SP101240: Ma = 1.14 ; NTR = 1.78

Fig. 18 Comparison of noise spectra obtained from LAVA-WMLES simulations with experiments by Bridges *et al.*. All simulations use a consistent FWH surface triangulation. Averaging over 72 observers in azimuth is applied for each polar angle at 90 deg (red) and 135 deg (blue).

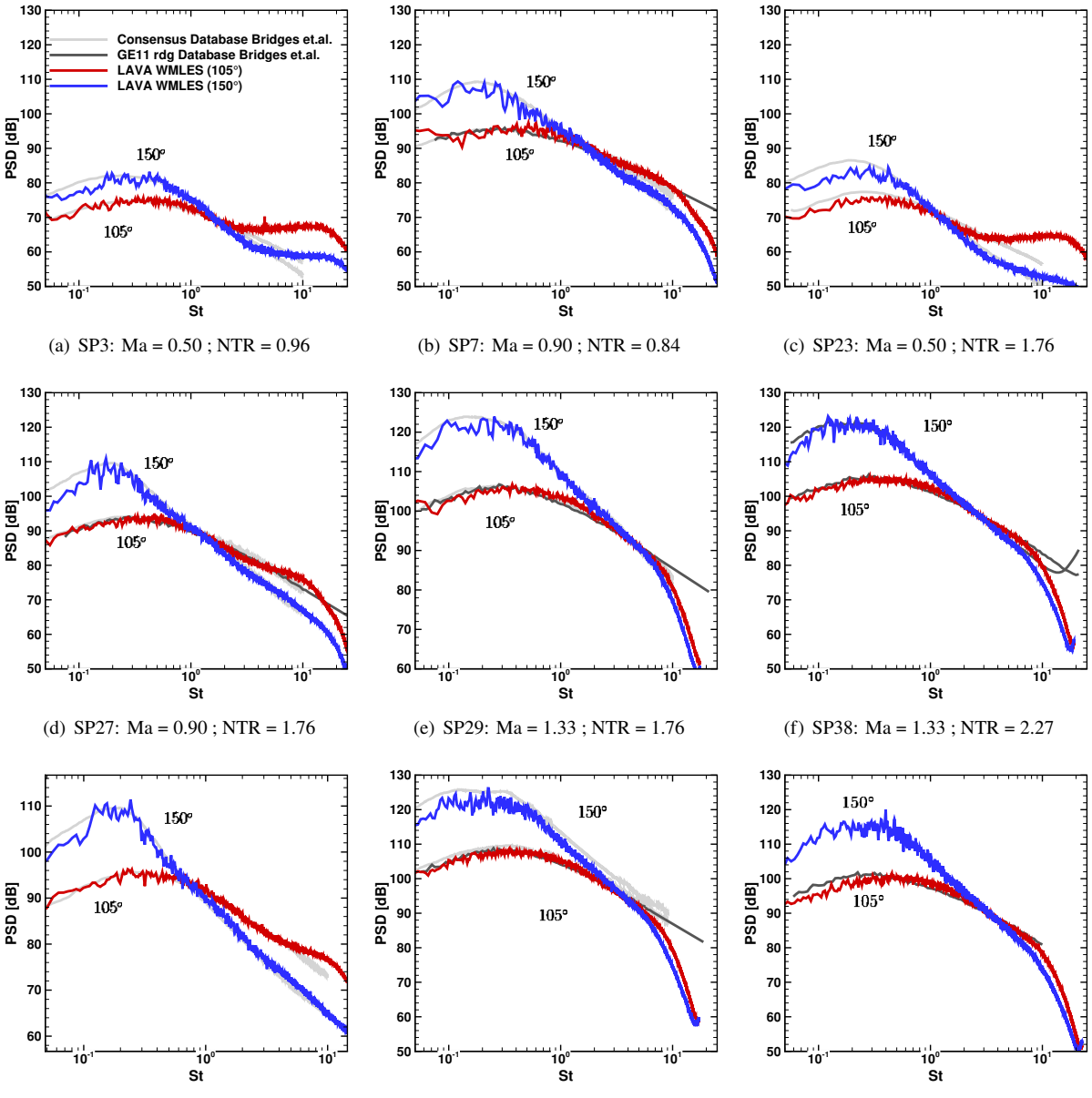

(a) SP3: Ma = 0.50 ; NTR = 0.96

(b) SP7: Ma = 0.90 ; NTR = 0.84

(c) SP23: Ma = 0.50 ; NTR = 1.76

(d) SP27: Ma = 0.90 ; NTR = 1.76

(e) SP29: Ma = 1.33 ; NTR = 1.76

(f) SP38: Ma = 1.33 ; NTR = 2.27

(g) SP46: Ma = 0.90 ; NTR = 2.70

(h) SP49: Ma = 1.48 ; NTR = 2.70

(i) SP101240: Ma = 1.14 ; NTR = 1.78

Fig. 19 Comparison of noise spectra obtained from LAVA-WMLES simulations with experiments by Bridges *et al.*. All simulations use a consistent FWH surface triangulation. Averaging over 72 observers in azimuth is applied for each polar angle at 105 deg (red) and 150 deg (blue).

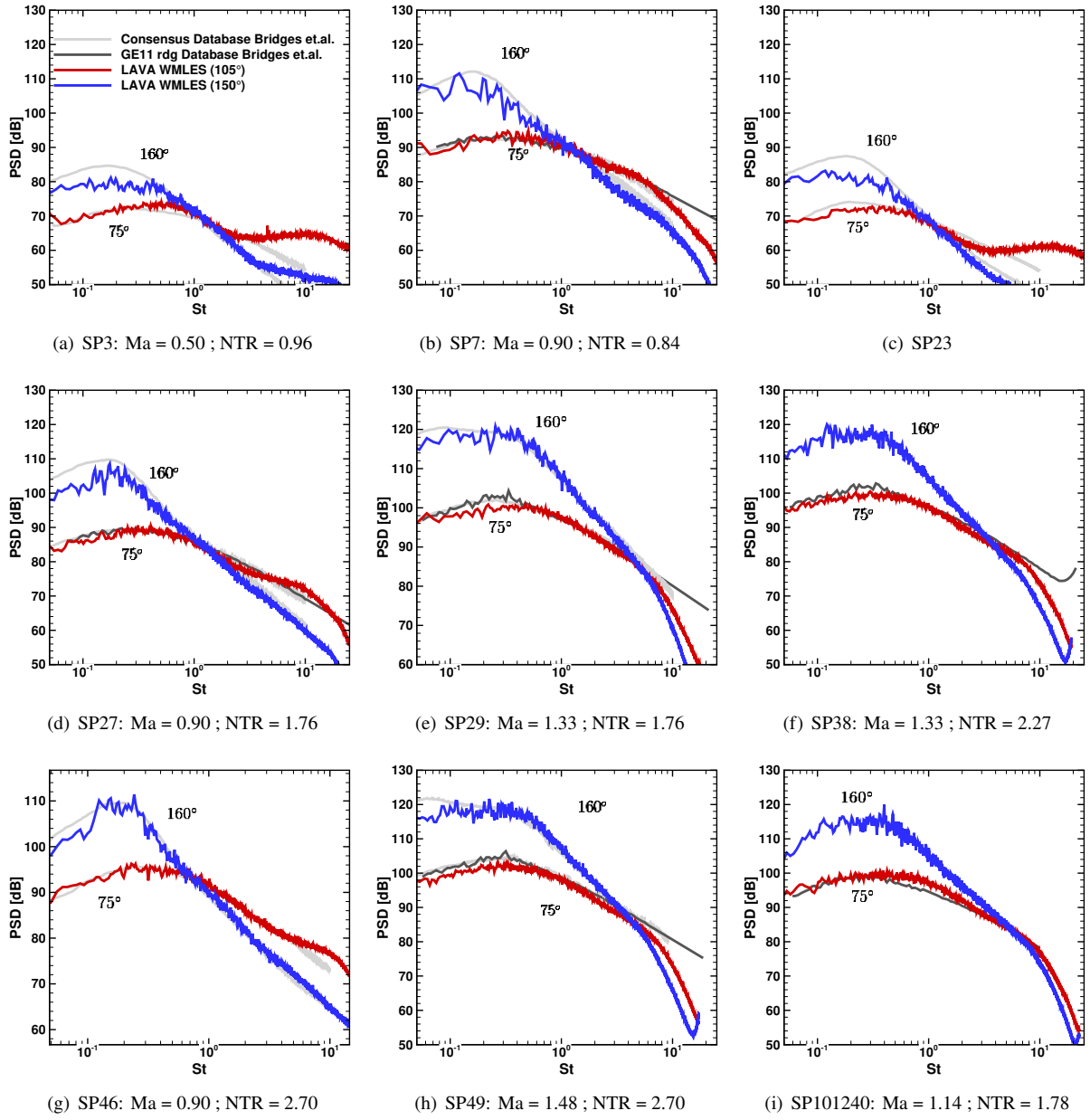

(a) SP3: Ma = 0.50 ; NTR = 0.96 (b) SP7: Ma = 0.90 ; NTR = 0.84 (c) SP23

(d) SP27: Ma = 0.90 ; NTR = 1.76 (e) SP29: Ma = 1.33 ; NTR = 1.76 (f) SP38: Ma = 1.33 ; NTR = 2.27

(g) SP46: Ma = 0.90 ; NTR = 2.70 (h) SP49: Ma = 1.48 ; NTR = 2.70 (i) SP101240: Ma = 1.14 ; NTR = 1.78

Fig. 20 Comparison of noise spectra obtained from LAVA-WMLES simulations with experiments by Bridges *et al.*. All simulations use a consistent FWH surface triangulation. Averaging over 72 observers in azimuth is applied for each polar angle at 75 deg (red) and 160 deg(blue).

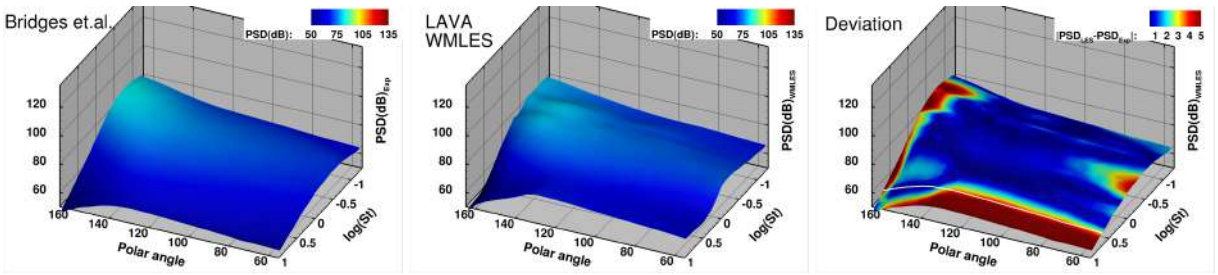

(a) SP3: Ma = 0.50 ; NPR = 1.197 ; NTR = 0.96

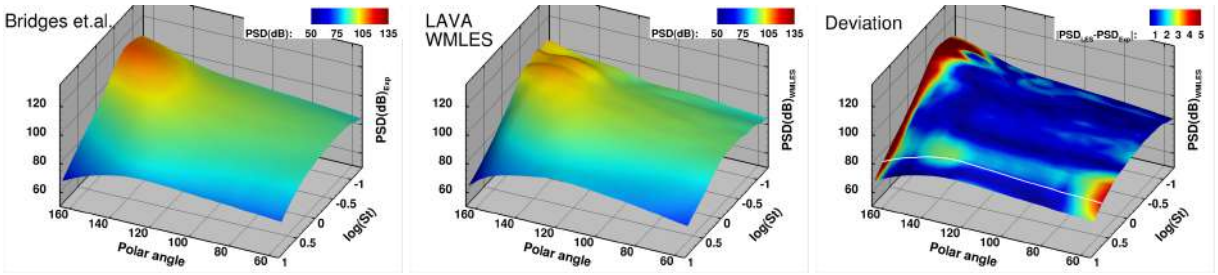

(b) SP7: Ma = 0.90 ; NPR = 1.852 ; NTR = 0.84

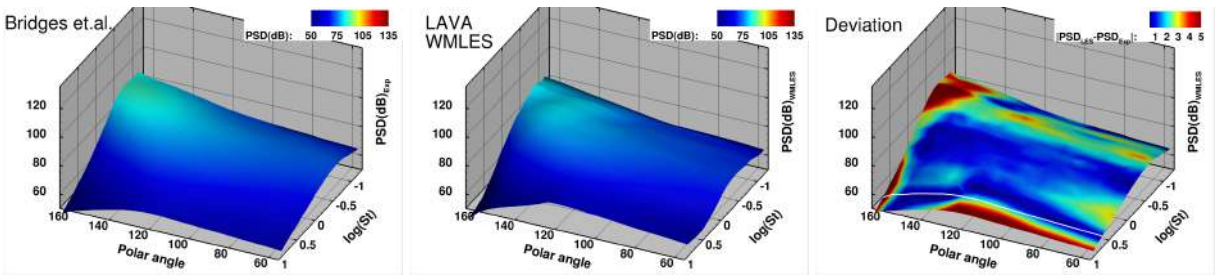

(c) SP23: Ma = 0.50 ; NPR = 1.852 ; NTR = 1.76

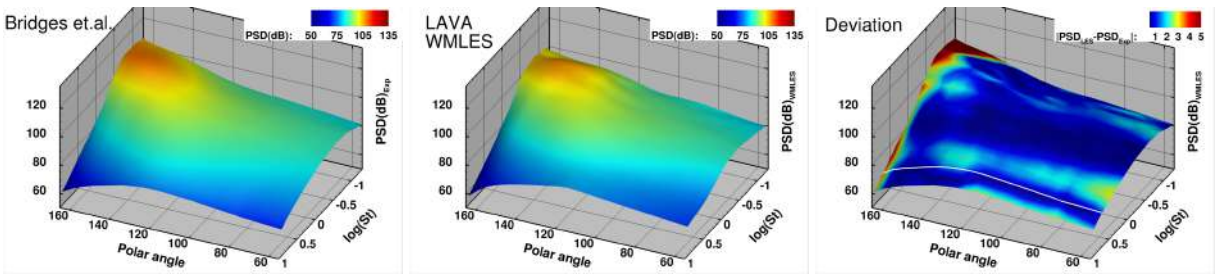

(d) SP27: Ma = 0.90 ; NPR = 1.368 ; NTR = 1.76

Fig. 21 Visual depiction of spectral directivity of far-field noise at 100D. Comparison of WMLES with Experiments by Bridges *et al.* [33]. Experimental and simulation narrow-band spectrum was converted to 1/3rd octave band frequency for a smoother signal. Third row shows experimental PSD contour plot colored by absolute of difference between experiment and simulation.

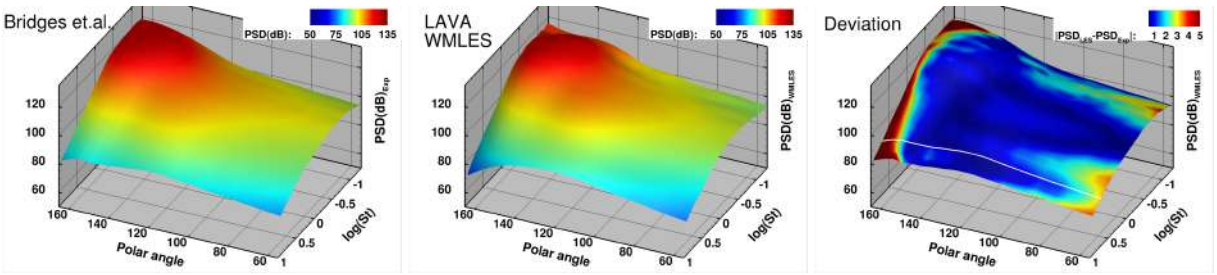

(a) SP29: Ma = 1.33 ; NPR = 1.898 ; NTR = 1.76

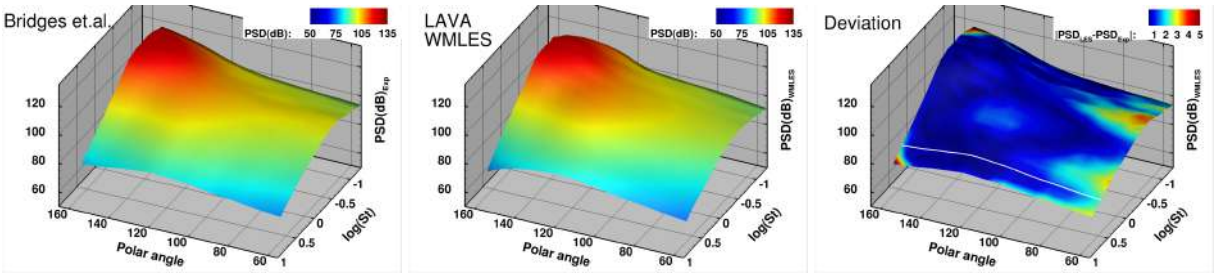

(b) SP38: Ma = 1.33 ; NPR = 1.664 ; NTR = 2.27

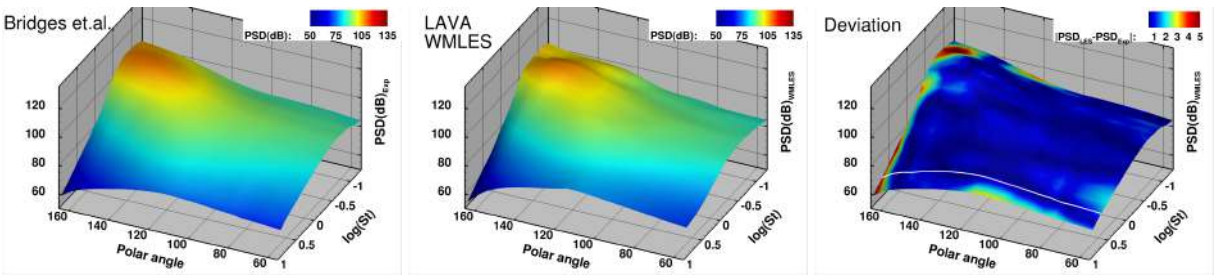

(c) SP46: Ma = 0.9 ; NPR = 1.219 ; NTR = 2.70

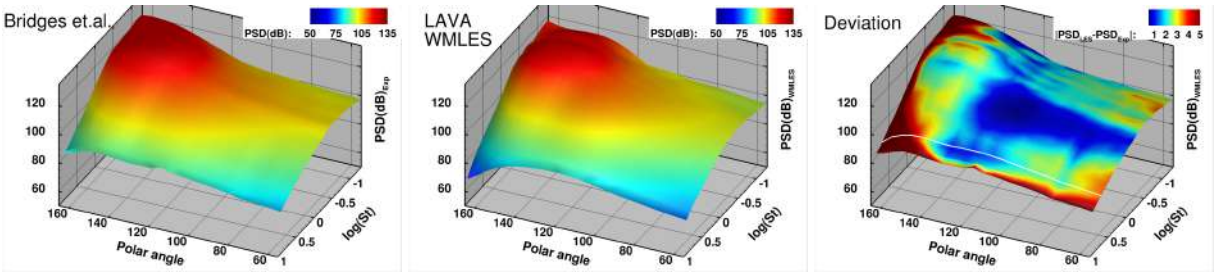

(d) SP49: Ma = 1.48 ; NPR = 1.697 ; NTR = 2.70

Fig. 22 Visual depiction of spectral directivity of far-field noise at 100D. Comparison of WMLES with Experiments by Bridges *et al.* [33]. Experimental and simulation narrow-band spectrum was converted to 1/3rd octave band frequency for a smoother signal. Third row shows experimental PSD contour plot colored by absolute of difference between experiment and simulation.

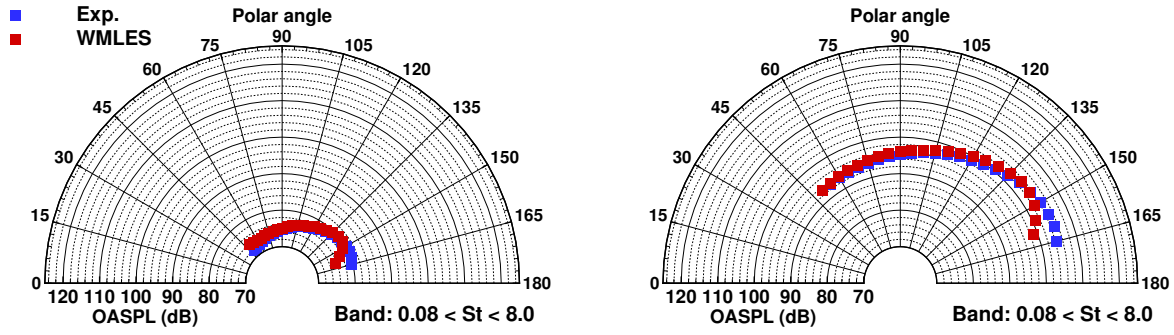

(a) SP3: Ma = 0.50 ; NTR = 0.96

(b) SP7: Ma = 0.90 ; NTR = 0.84

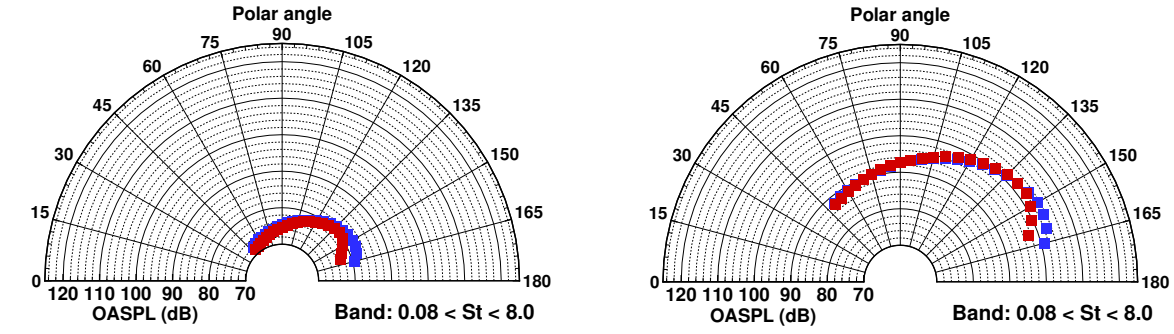

(c) SP23: Ma = 0.50 ; NTR = 1.76

(d) SP27: Ma = 0.90 ; NTR = 1.76

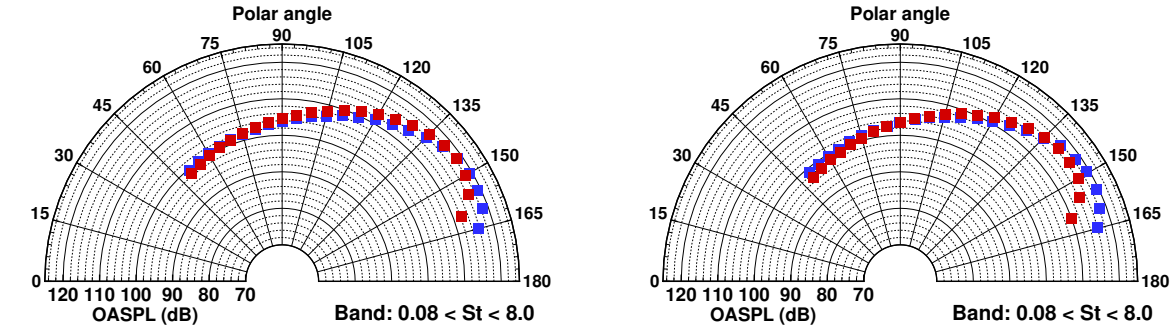

(e) SP29: Ma = 1.33 ; NTR = 1.76

(f) SP38: Ma = 1.33 ; NTR = 2.27

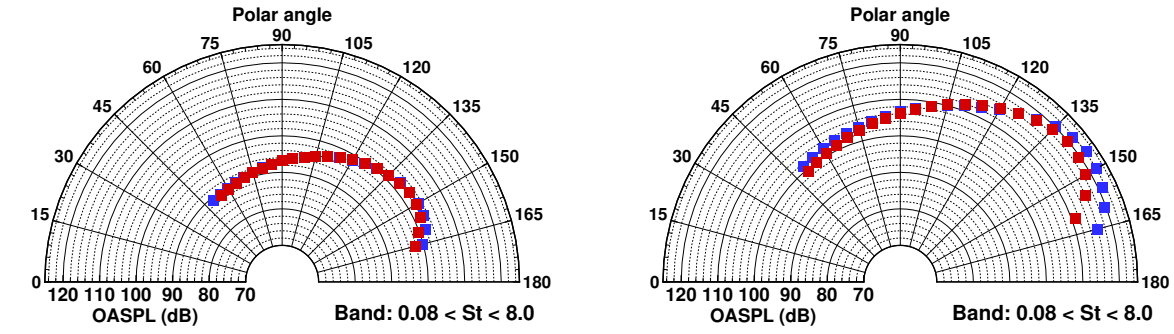

(g) SP46: Ma = 0.90 ; NTR = 2.70

(h) SP49: Ma = 1.48 ; NTR = 2.70

Fig. 23 Comparison of band limited (0.05 < St < 8) overall sound pressure levels at 100D from the nozzle exit obtained from WMLES with FWH propagation with experiments by Brown and Bridges [36].